BULLETIN OF MATERIALS SCIENCE AND METALLURGY

Volume 1 I Issue 1 I Pages 1-30 I JAN 2024

ONLINE ISSN:3023-6509

bulletinofmsm.org/

Periodical Scientific Journal of UCTEA Chamber of Metallurgical and Materials Engineers

BMSM

BULLETIN OF MATERIALS SCIENCE AND METALLURGY
Periodical Scientific Journal of UCTEA Chamber of
Metallurgical and Materials Engineers

TMMOB Metalürji ve Malzeme Mühendisleri Odası Metalürji ve Malzeme Dergisi ücretsiz ekidir. Anı sayısıdır, bir defaya mahsus basılmıştır.

İMTİYAZ SAHİBİ / PRIVILEGE OWNER
Ahmet İrfan TÜRKKOLU
TMMOB Metalürji ve Malzeme Mühendisleri Odası Adına
Yönetim Kurulu Başkanı

SORUMLU YAZI İŞLERİ MÜDÜRÜ / PRODUCTION DIRECTOR
Alişan YILMAZ
İzmir Şube Yönetim Kurulu Sekreteri

JOURNAL MANAGEMENT AND CORRESPONDENCE ADDRESS
TMMOB Metalurji ve Malzeme Mühendisleri Odası
Kültür Mahallesi, Çaldıran Sokak Nida Apt. No:14/13 Kolej,
Çankya / ANKARA
Tel: 0312 425 41 60
e-posta: oda@metalurji.org.tr
http:/www.metalurji.org.tr

TEKNİK SORUMLU / TECHNICAL ASSISTANT

Umur Berkan ÇELİK

PREPARES FOR PRINTING / BASIMA HAZIRLAYAN
Adresist Reklamcılık
Hatboyu Cad. No: 6/38 Bakırköy/istanbul
Tel: 0533 369 23 29
www.adresist.com

BASKI/PRINTED BY
Elit Ofset Matbaacılık, Ambalaj San. ve Tic. A.Ş.
İkitelli Org. San. Böl. ipkas Sanayi Sitesi 3.Etap B 19 Blok No:5
Küçükçekmece/ İstanbul
Tel: 0212 549 88 60 - Faks: 0212 549 88 65 www.elitofset.com

BASKI SAYISI / CIRCULATION
1250

BASKI TARİHİ / PUBLISHING DATE
29 Ağustos 2024

BULLETIN OF MATERIALS SCIENCE AND METALLURGY

BULLETIN OF MATERIALS SCIENCE AND METALLURGY

BULLETIN OF MATERIALS SCIENCE AND METALLURGY

BULLETIN OF
MATERIALS SCIENCE AND METALLURGY

CONTENTS

Investigation of atmospheric corrosion of 6063 aluminium alloy in industrial environment
Emre Çankaya*, Alptuğ Tanses, İ. Artunç Sarı, Görkem Özçelik
Page: 1 - 5

Investigation of production conditions of interstitial-free steels in electric arc furnace
Ali Cem Taşdemir*, Onuralp Yücel
Page: 6 - 10

Effect of Calcination Temperature on Crystalline phase and Grain size of ZnO Particles
Mahla Shahsavar Göçmen*, Gabriel Uğurgel, Yiğit Gül, Enes Barış Bilge, Ömer Faruk Uslu, Umut Doğan Gürkan, Gökçe Çiçek Kaya, Mithat Emre Şahbazoğlu, Batuhan Yıldız, Gurur Unan, Kris Terzioğlu, Ayşe Dulda
Page: 11 - 15

Imprinting Bone Surface Topography on Cast Metal
Aybüke Üretmen*, Caner Demir, Vram Odabaşıoğlu, Abdulhalim Kılıç
Page: 16 - 22

Carbon Capture Performance Enhancement of Solid State Synthesized Li4SiO4 Powders by Using Different Kind Steel Slags as SiO2 Source
Fatih Kutay Mete, Kağan Benzeşik*, Ahmet Turan, Maria Teresa Izquierdo, Onuralp Yücel
Page: 23 - 30

BMSM

Bulletin of Materials Science & Metallurgy

Periodical Scientific Journal of UCTEA Chamber of Metallurgical and Materials Engineers

Volume 1, Issue 1, 2024, Pages 1-5 Received: 16.01.2023 Revised: 20.06.2023 Accepted: 22.01.2024

Research Article

Investigation of atmospheric corrosion of 6063 aluminium alloy in industrial environment

Emre Çankaya*, Alptuğ Tanses, İ. Artunç Sarı, Görkem Özçelik

ASAS Aluminium

*Corresponding author's email: emre.cankaya@asastr.com

Abstract

Demand for aluminium alloys is increasing day by day, especially with the electrification trend of the automotive industry. The reason for this increase lies in the advantages of aluminium such as high specific strength, low density, high recyclability and high corrosion resistance. Especially corrosion behaviour is important for aluminium parts used in structural components. High corrosion resistance in aluminium alloys stem from its natural oxide layer. Although this layer provides a certain level of corrosion resistance, it cannot completely prevent corrosion. Exclusively in industrial environment, aluminium alloys are more corroded due to the high presence of corrosive substances such as moisture, dust, dirt and chemicals. Aluminium specimens were left next to ASAŞ Aluminium anodizing facility which has air containing H_2SO_4, moisture, dust and dirt. Due to high volatile chemicals around anodization facility, this location has been selected to place the samples. To examine and compare the corrosion degrees, 3-, 6- and 12-months exposing times were selected. In this study, corrosion behaviour of the 6063 aluminium profiles placed at same zone with different waiting times in industrial environment was investigated. In order to make comparisons, samples were examined under optical microscope and SEM. At 6 months samples, the corrosion type change has been examined from pitting to IGC. This study is done in order to minimize the scrap amount causing from atmospheric corrosion after anodization of structural automotive profiles.

Keywords

Corrosion, anodised aluminium, 6063 alloy, IGC, pitting

1. Introduction

The atmospheric corrosion behaviour of aluminium alloys is well understood, thanks to decades of observance of old structures. The church of San Gioacchino is one of these observed structures. In addition, long-term corrosion tests performed open air since 1935 (especially in the marine and industrial environment) are also important in determining the corrosion behaviour of aluminium alloys [1].

Performing corrosion tests in a laboratory environment can give an idea about the corrosion behavior of the material, but in order to simulate real life, it is necessary to see its behavior in ambient conditions. Intergranular and pitting corrosion type are most popular for atmospheric environment [2-5].

Atmospheric environment is divided into 4 categories: Rural, Urban, Industrial and Marine [6].

Temperate industrial regions where this study also carried out are characterized as very strong in terms of corrosion aggression [6].

Mostafa Sliem et al. investigated the corrosion behaviour of 6082 and 6063 alloys in the Qatar region. According to the study findings, it has been observed that these alloys tend to inherit intergranular corrosion (IGC) in the industrial environment. In addition, it was stated that the chloride ions in the environment affect the pitting corrosion rate [7].

M. Merajul Haque et al. examined corrosion behaviour of galvanized steel compared with aluminium in %5 NaCl solution Fig. 1 shows the corrosion behaviour of galvanized steel and aluminium. Aluminium has a clear corrosion behaviour advantage over galvanized steel is seen here [8].

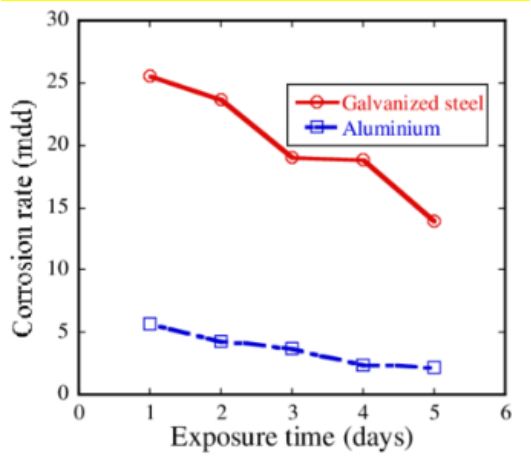

Figure 1. Corrosion behaviour of galvanized steel and aluminium [8].

Aluminium is an amphoteric metal which means it can react with both acids and bases which means it can be corroded by both this is why we have left the samples near anodization facility which contains both acids and bases. Also, Pongsaksawad, Wanida et al. have been conducted 6005A and 6082 alloy corrosion test for 18 months period [9,10].

In this study, atmospheric corrosion behaviour of 6063 alloy in the industrial environment (ASAS Aluminium production plant, Sakarya, Turkey) was investigated for 3 months, 6 months and 12 months of periods.

2. Materials and Methods

2.1. Materials

Since it is one of the most widely used 6xxx series aluminum alloy, 6063 alloy is preferred in this study.

Table 1 shows OES analysis of 6063 aluminium specimen.

Table 1. Chemical composition (wt.%) of 6063-T6 alloy.

Element	Si	Mg	Fe	Cu	Mn	Zn	Al
Weight Fraction (%)	0,50	0,55	0,17	0,01	0,02	0,01	Bal.

2.2. T6 Heat Treatment Procedures

T6 condition include solution treatment and artificial aging steps. Artificial aging temperature is 185°C, time is 5,5 hours for all specimens.

2.3. Method

Aluminium profiles have been studied for periods of 3, 6 and 12 months. The specimens were cut using a saw with oil based cooling system.

Heat treated profiles then left in the corrosive industrial environment. Aluminium specimens were exposed to atmospheric corrosion next to ASAŞ Aluminium anodizing facility. The environment which has been claimed to have has been its air analysed and in conclusion it contained H_2SO_4, and high amounts of humidity throughout the experiment.

Corroded profiles then collected in the predetermined times and after cleaning the surface of the profile, technical anodizing operation was carried out. The thickness of the anodizing layer is approximately 10 μm. In order to determine the corrosive environment's effect on the material, all specimen has been analysed under optical microscopy, Scanning Electron Microscopy (SEM). Energy Dispersive Spectrometer (EDS) analysis has also been done to the corroded spots.

3. Results and Discussion

3.1 Optical Microscope Analysis

Corroded profiles taken from facility area at 3,6 and 12 months investigated via Optical Microscope.

Fig. 2,3 and 4 show that optical microscope images of 3-6-12 months waited profiles respectively.

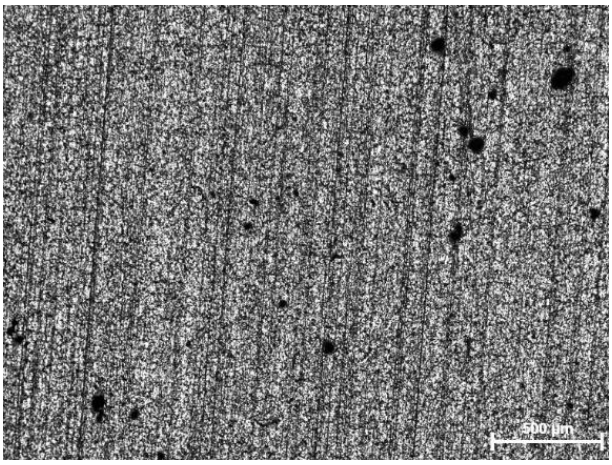

Figure 2. Optical Microscope image of 3 months waited profile (100x).

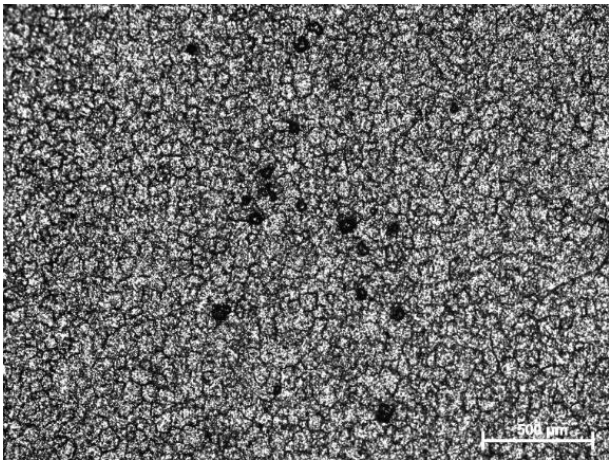

Figure 3. Optical Microscope image of 6 months waited profile (100x).

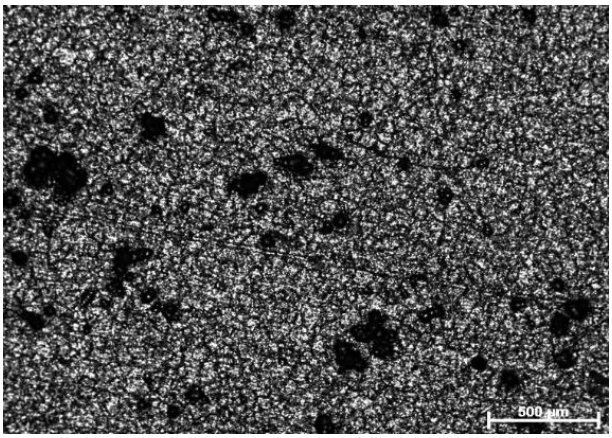

Figure 4. Optical Microscope image of 12 months waited profile (100x).

In Fig. 2 Number of pits are low and dimension are relatively small. The dominant corrosion type is pitting corrosion here. As the time progresses to 6 months, number of pits increased and also intergranular corrosion starts to damage material as seen in Fig. 3.

When the time is increased to 12 months in Fig. 4 size and number of the pits are the highest as expected. It is seen that, IGC has been progressing and weakening the material in the process.

3.2 SEM Analysis

After metallographic preparation, cross section of the sample was investigated in SEM and surface analysis was carried out in order to characterize frequency of corrosion. Fig. 5,6 and 7 show 3-6-12 months waited profiles' surface images under SEM, respectively.

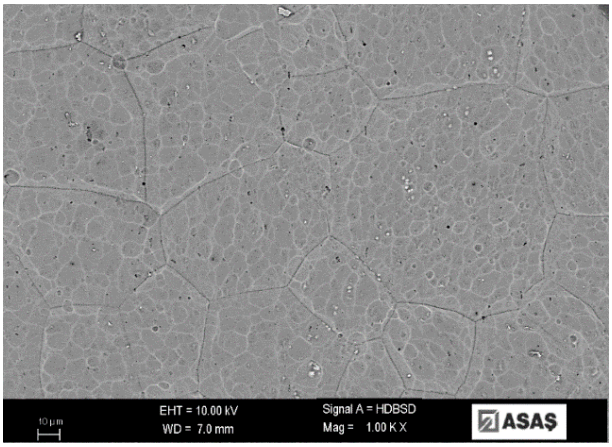

Figure 5. SEM image of 3 months waited profile (1000x).

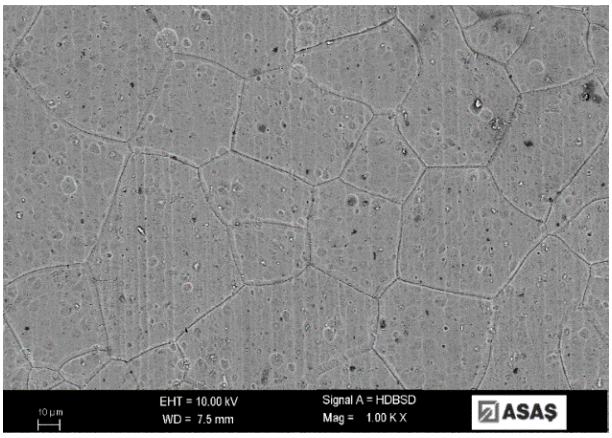

Figure 6. SEM image of 6 months waited profile (1000x).

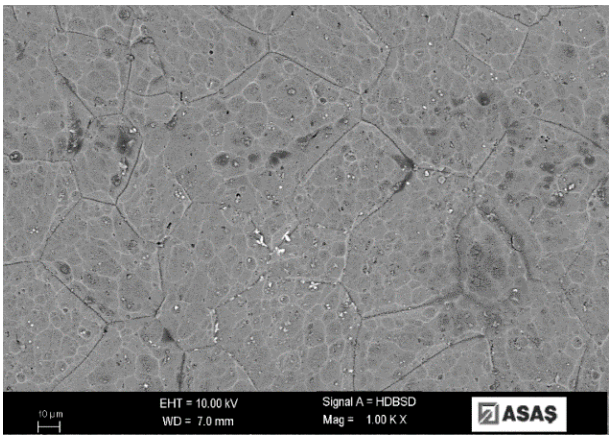

Figure 7. SEM image of 12 months waited profile (1000x).

When examined Fig. 5-7, pits are prominently visible under anodized layer and their number is increased with exposure time. As shown in Fig. 7, longer waiting time increases corrosion degree due to acid, base and humidity factors.

Fig. 8,9 and 10 show 3-6-12 months waited profiles' cross sections images under SEM, respectively.

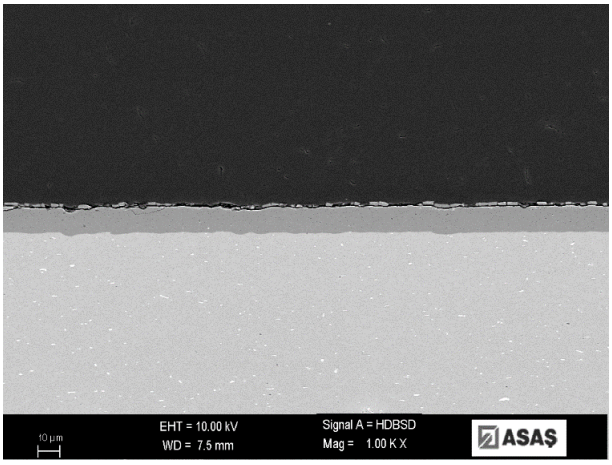

Figure 8. SEM cross section image of 3 months waited profile (1000x).

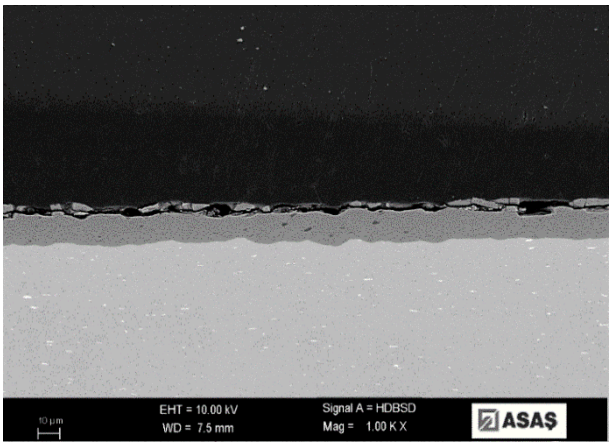

Figure 9. SEM cross section image of 6 months waited profile (1000x).

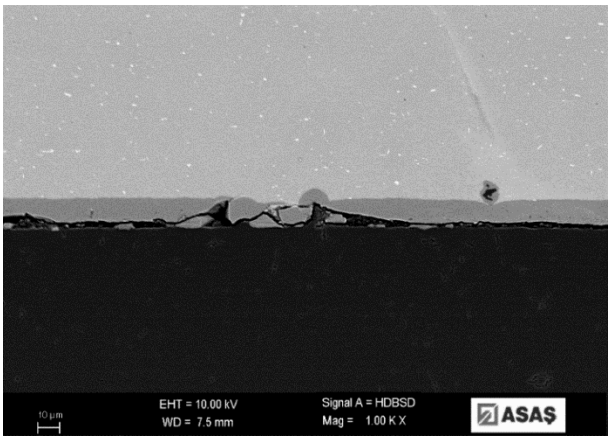

Figure 10. SEM cross section image of 12 months waited profile (1000x).

In Fig. 8-10 damage on the surface caused by pitting corrosion is observed. The deepest damage can be seen in Fig. 10 from the damage under the anodizing layer.

3.3 EDS Analysis

EDS Analysis was performed from the corrosion pit. Analysis result and selected area given in Fig. 11.

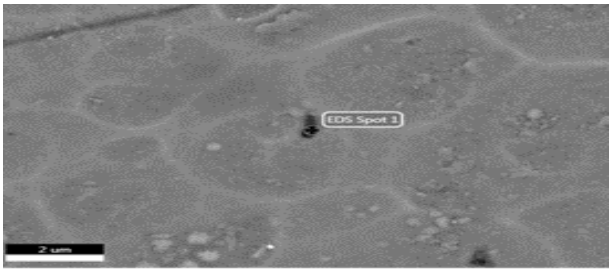

Element	Weight %	Atomic %	Error %
O K	8.29	13.49	10.63
Al K	78.85	76.07	2.82
S K	12.85	10.43	8.00

Figure 11. EDS Analysis Selected Area and Elemental Analysis Results.

In the EDS analysis taken from the corrosion pit in Fig. 11, the presence of Oxygen and Sulphur element is thought to be caused by oxidized aluminium and sulfuric acid in the environment during anodization process.

EDS Spectra of the selected zone is given in Fig. 12.

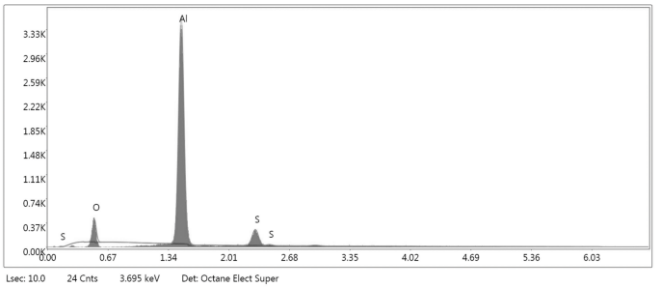

Figure 12. EDS Spectra of Selected Area.

4. Conclusion

Results obtained from this work indicate a significant effect of the atmospheric conditions and waiting time on corrosion performance of aluminium.

(1) Pitting corrosion starts after 3 months exposure to atmosphere.

(2) When exposure time is up to 6 months, pitting and IGC co-existed on the surface due to the presence of weak areas on the natural oxide layer.

(3) After exposure for 12 months, the natural aluminium oxide layer had lost its protective effect completely and IGC and pitting corrosion intensity increased during corrosion period.

Authors' Contributions

Designing and writing: Emre Çankaya; materials preparation, and characterization: Alptuğ Tanses; revision and technical support: İlyas Artunç Sari and Görkem Özçelik.

Declaration of Competing Interest

The authors declare that they have no known competing financial interests or personal relationships that could have appeared to influence the work reported in this paper.

Acknowledgement

We would like to thank Samet Sevinç in microscopic examinations and ASAŞ Aluminium R&D department for their support.

References

[1] C. Vargel, "Resistance of aluminium to atmospheric corrosion" in Corrosion of Aluminium, C. Vargel, Ed., Elsevier, 2020, ch. 5, pp. 575-589.

[2] Shuangqing Sun, Qifei Zheng, Defu Li, Junguo Wen, Long-term atmospheric corrosion behaviour of aluminium alloys 2024 and 7075 in urban, coastal and industrial environments, Corrosion Science, Volume 51, Issue 4, 2009, Pages 719-727, ISSN 0010-938X, https://doi.org/10.1016/j.corsci.2009.01.016.

[3] W.J. Liang, P.A. Rometsch, L.F. Cao, N. Birbilis, General aspects related to the corrosion of 6xxx series aluminium alloys: Exploring the influence of

Mg/Si ratio and Cu, Corrosion Science, Volume 76, 2013, Pages 119-128, ISSN 0010-938X, https://doi.org/10.1016/j.corsci.2013.06.035.

[4] Sheng Zhang, Teng Zhang, Yuting He, Daoxin Liu, Jipu Wang, Xu Du, Binlin Ma, Long-term atmospheric corrosion of aluminum alloy 2024-T4 in coastal environment: Surface and sectional corrosion behavior, Journal of Alloys and Compounds, Volume 789, 2019, Pages 460-471, ISSN 0925-8388, https://doi.org/10.1016/j.jallcom.2019.03.028.

[5] Tao J, Xiang L, Zhang Y, Zhao Z, Su Y, Chen Q, Sun J, Huang B, Peng F. Corrosion Behavior and Mechanical Performance of 7085 Aluminum Alloy in a Humid and Hot Marine Atmosphere. Materials (Basel). 2022 Oct 26;15(21):7503. doi: 10.3390/ma15217503. PMID: 36363095; PMCID: PMC9655200.

[6] Z. Ahmad, "Atmospheric Corrosion" in Principles of Corrosion Engineering and Corrosion Control, Z. Ahmad, Ed., Butterworth-Heinemann, 2006, ch. 10, pp. 550-575,

[7] M. Sliem, A. Aboubakr, A.M.A. Mohamed, R. Demian and Johnson, Roy. (2015). Atmospheric corrosion behaviour of 6xxx Al alloys in Qatar State.

[8] M. Merajul Haque, S. Alam Limon, Md. Moniruzzaman and Md. Mohar Ali Bepari, "Corrosion Comparison of Galvanized Steel and Aluminum in Aqueous Environments", Int. J. Automot. Mech. Eng., vol. 9, pp. 1758–1767, Dec. 2022.

[9] Prabhu Deepa, Rao Padmalatha, Corrosion behaviour of 6063 aluminium alloy in acidic and in alkaline media, Arabian Journal of Chemistry, Volume 10, Supplement 2, 2017, Pages S2234-S2244, ISSN 1878-5352, https://doi.org/10.1016/j.arabjc.2013.07.059.

[10] Pongsaksawad, Wanida, He, Jiajie, Li, Chuanying, Klomjit, Pitichon, Khamsuk, Piya, Wang, Rui, Wangjina, Pranpreeya, Sun, Xiaoguang and Viyanit, Ekkarut. "Atmospheric corrosion behaviors of 6000-series aluminum alloy under tropical climate influences of Thailand" Materials Testing, vol. 65, no. 6, 2023, pp. 924-933. https://doi.org/10.1515/mt-2022-0325.

BMSM

Bulletin of Materials Science & Metallurgy

Periodical Scientific Journal of UCTEA Chamber of Metallurgical and Materials Engineers

Volume 1, Issue 1, 2024, Pages 6-10 Received: 31.01.2023 Revised: 01.09.2023 Accepted: 22.01.2024

Research Article

Investigation of production conditions of interstitial-free steels in electric arc furnace

Ali Cem Taşdemir*, Onuralp Yücel

Department of Metallurgical and Materials Engineering, İstanbul Technical University, İstanbul, Turkey

*Corresponding author's email: tasdemir20@itu.edu.tr

Abstract

The iron and steel industry has had a strategic importance throughout history. In recent years, with the development of technology and sectoral competition, new investments have been investigated. One of them is Interstitial-Free (IF) steels. Interstitial-Free Steel, containing very small amounts of carbon and nitrogen, is used in the production of automotive interior and exterior panels. IF steel structures have high formability. This feature has been obtained by removing interstitial atoms such as C and N in vacuum degassing method. In addition, remaining of these elements can be stabilized in steel by adding Ti and/or Nb. After the steel production process is completed, the slab is heated to a certain temperature in the heating furnace. The finishing and coiling temperatures are also important factors in determining the deep-drawing capability. These parameters help in obtaining the coarse TiC and NbC precipitates and the high r value, which is an important indicator of fine-grained structure, high ductility and formability. In this study, the effect of process parameters on IF steels in electric arc furnace steel production, secondary metallurgy processes and hot rolling are explained. Also, the effect of microstructures of steel samples with different chemical compositions and thicknesses on mechanical properties was investigated. In addition, the samples taken from the hot rolled coil were examined under scanning electron microscope (SEM), and texture analysis was performed with electron backscatter diffraction (EBSD) technique. Particularly, the microstructure investigations have shown that Ti and/or Nb is the critical element in terms of ensuring the formability, so interstitial atoms are not formed.

Keywords

Continuous Slab Casting; Electric Arc Furnace; Hot Rolling; IF steels; Ladle Furnace; Metallurgy

1. Introduction

The term 'interstitial steel or IF steel' means that there are no interstitial atoms (C and N) in the lattice structure and the resulting steel is mild steel [1]. Thus, it is prevented that the precipitates inhibit the movement of grain boundaries during recrystallization [2].

IF steels have a body-centred cubic (bcc) crystal lattice structure, have a ferrite phase. The ferrite grain size in the structure affects the yield strength, ductility and strain hardening exponent (n). The main properties of these steels are low yield strength, high plastic anisotropy ratio (r value), low aging property, good deep drawing and good formability. After hot deformation, cold rolling and annealing, a recrystallization texture {111} is formed, where high deformation occurs. This type of texture allows high levels of r, which is associated with good formability of ultra-low carbon [1].

2. Production of IF Steels

2.1. Steel Production in Electric Arc Furnace

Steel melting takes place in an electric arc furnace. Scrap (HBI, Pig iron and DKP) is used as charging material. The most basic task of the furnace is to facilitate the next processes by providing rapid melting. After the scrap charge is transferred to the furnace, the furnace door is closed and the electrodes form an arc in the furnace with the voltage given by the system. Oxygen and carbon are blown from the burners and then the steel is refined. After the steel melting process is completed, impurities are formed and lime, pyramid Al, ferromanganese are added to remove these impurities from the steel and take them into the slag. Due to the high temperatures reached in the electric arc furnace, phosphorus is removed from the steel by binding to the slag with lime. The amount of sulphur is reduced from 0.080 - 0.090% to 0.010 - 0.008%.

$$2P + (5FeO) + 3(CaO) = 3CaO.P_2O_5 + 5Fe \quad T < 1570^{o}C \quad (1)$$

After the scrap smelting and refining processes are completed in the electric arc furnace, it is time for the tilting process. The purpose of tilting is to separate slag and steel from each other. The slag taken from the furnace is sent to the slag plant, while the steel is sent to the ladle furnace. Casting temperature is in the range of 1600-1620°C [3].

2.2. Ladle Furnace

Secondary Metallurgy or Ladle Metallurgy as it is commonly used covers all metallurgical processes such as heating of molten steel, deoxidation, desulfurization, composition adjustment, homogenisation, flotation of inclusions and degassing.

Liquid steel is transferred to the ladle. After the centring process of the ladle is completed, the magnetic stirrer and gas blowing system are kept open until the entire process is completed. The ladle must first be deoxygenated. Ca, Mn, Si and Al are added to the ladle for deoxidation. After the addition of Al ingot, titanium alloys are added to the liquid steel [4].

One of the other materials added to the ladle is lime. The purpose of the lime material here is to increase the alkalinity in the ladle to obtain basic slag and to remove the sulphur. The removal of sulphur by the slag reaction is shown below:

$$CaO + S \rightarrow CaS + 1/2\ O_2 \quad (2)$$

The steel that reaches the desired alloy values is taken from the ladle furnace and sent to the vacuum degassing section [4].

2.3. Vacuum Degassing

The degassing process starts with placing the ladle with liquid steel inside the vacuum tank and argon gas is sent during the vacuum process. The ladle pressure under vacuum drops to 0.5 mbar. The mixing process under vacuum conditions is achieved by the [C]+[O] = {CO} reaction starting in the steel. Hydrogen is the most important gas to be removed during the vacuum degassing process. Liquid steel, which contains about 8 ppm of hydrogen, contains 2 ppm of hydrogen at the end of the vacuum. Cleaner, lower carbon steel is obtained after vacuum.

2.4. Continuous Slab Casting

Continuous casting is the process in which the metallurgically optimized liquid steel is continuously solidified into a slab after being passed through a moving mould cavity.

The realization stages of a slab casting are as follows and are shown schematically.

Ladle (liquid steel)→Turret→Tundish→Moulding→Pull-Straightening Unit→Cutting

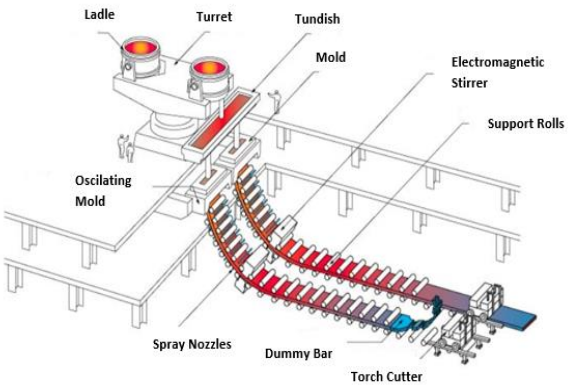

Figure 1. Typical Process Layout; Two-strand Continuous Slab Caster [5].

The liquid steel in the ladle is placed in the turret and poured into the tundish. From the nozzles under the tundish, the liquid steel flows into the mould and is solidified as slab.

The casting machine works with a closed casting system. In this way, liquid steel flows through the refractory tubes and sealing is ensured. The aim here is to cut the contact of the steel with the air and to prevent the formation of inclusions or steel pollution by direct oxidation with O2 in the air.

2.5. Hot Rolling

Slabs are heated up to 1250°C in slab heating furnaces. The slabs coming out of the furnace come to the descale (scale removal). The scale on the slab is cleaned by spraying 210 bar of water. Rolling is done in 5 or 7 passes in the reversibly working quartet mills. The temperature drops from 1250°C to 1140°C. The slab from the roughing mill arrives in the coil box and is rolled. The aim here is to save space and to provide heat homogenization by reducing the surface area. The material that is opened after the coil box and to be taken to the strip mill comes to the crop shear before the strip mill and the uneven coil head and end parts are cut. Afterwards, cleaning is done in secondary descaling. The slab arriving at the strip mill continues to be rolled and its temperature is approximately 960°C. The final thickness of the strip is also given on a 7-foot strip mill.

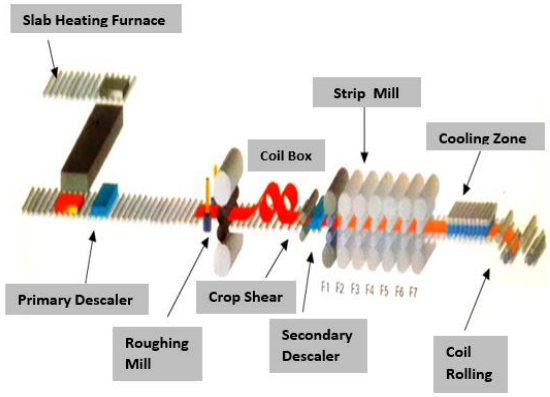

Figure 2. Hot Rolling Process [5].

3. Hot Rolling Parameters

The basic hot rolling parameters that determine the microstructure and mechanical properties of the steel grades to be annealed in the continuous annealing line are as follows:

• Slab Heating Temperature

• Finishing Temperature

• Coiling Temperature

3.1. Slab Heating Temperature

Heating of the slab takes place in the slab furnaces and the dissolution of TiC and NbC precipitates occurs in the furnace. As a result of dissolution, the final hot band texture and grain size are determined. As the slab heating temperature decreases, higher ductility and r values are obtained in IF steels [6].

3.2. Finishing Temperature

In order to obtain a homogeneous microstructure product and to provide the desired mechanical properties, the transformation temperature must be greater than the A3 transformation temperature. In addition to the advantages of high finishing temperature to product quality, it has certain limitations as it causes scale (oxide layer) formation. The best cold rolled and annealed texture is obtained in hot rolled fine grain hot band at 30-80°C above the A3 temperature. As the supply temperature decreases, the grain size, % elongation, and deep drawability values also decrease [6].

3.3. Coiling Temperature

In IF steels, the rolling temperature is preferred high to accelerate ferrite grain growth, promote TiC and NbC formation, and complete precipitation of AlN [5]. As the rolling temperature increases, the % elongation increases, while the yield and tensile strength decreases. With the increase in temperature, the ferrite recrystallization {111} texture is improved and as a result, higher r values are provided [7].

4. Experimental Studies

In the experimental studies, 2 samples with 78-89% reduction ratios were taken from hot rolled Ti-containing IF coils. The rolled sheet sample with a thickness of 2 mm is named A1 and the rolled sheet sample with a thickness of 3 mm is named A2. In these samples, the effects of hot rolling parameters on mechanical properties and crystallographic texture were investigated. Basic chemical analyses of steels are given in Table 1.

Table 1. Chemical analyses of A1 and A2 samples

Sample Number	A1	A2
C	0,002	0,003
Mn	0,107	0,092
Si	0,015	0,012
Ti	0,064	0,061
N	0,007	0,007
P	0,009	0,007
S	0,008	0,004

In order to determine the mechanical properties of the IF quality steel coil, transverse (0°), longitudinal (90°) and diagonal (45°) samples were taken in different directions according to the rolling direction, and tensile tests were carried out with Zwick Z600 device and hardness tests with Zwick ZHU250 device. Samples with different hot rolling reduction ratios of 78% and 89% were polished and grinded for metallographic examinations. The internal structures of the bakelite were etched and examined in the Nikon Eclipse MA200 microscope. Nital solution consisting of 97.5 cc of ethanol and approximately 2.5 cc of nitric acid was used as etching agent in all samples.

5. Results and Discussion

Mechanical tests applied to hot rolled IF steel samples with different deformation rates (78-89%) were investigated. Although only Ti-containing A1 and A2 samples had similar chemical analyses, they showed different % elongation values(ε). The difference here shows that the increase in the reduction ratio causes a higher % elongation in the material. The strain hardening exponent (n) varies between 0.21 and 0.23, and no systematic changes were observed in yield, tensile strength and elongation at rupture.

Table 2. Tensile test results of samples

	Tensile Test Direction	**σ_a MPa**	**$\sigma_ç$ MPa**	**ε (%)**	**n**
A1	0^0	172	324	34,6	0,22
	90^0	183	329	38,7	0,23
	45º	243	321	37,0	0,23
A2	0^0	264	329	41,8	0,21
	90^0	246	329	44,1	0,22
	45º	248	321	47,7	0,23

The hardness test result is given in Table 3. The steel was mild steel (67-450 HB) according to the applied load degree (kp=30) and showed that the samples were IF steel according to the hardness measurement range.

Table 3. Hardness test results.

Sample	A1	A2
HB	92.4	99.0

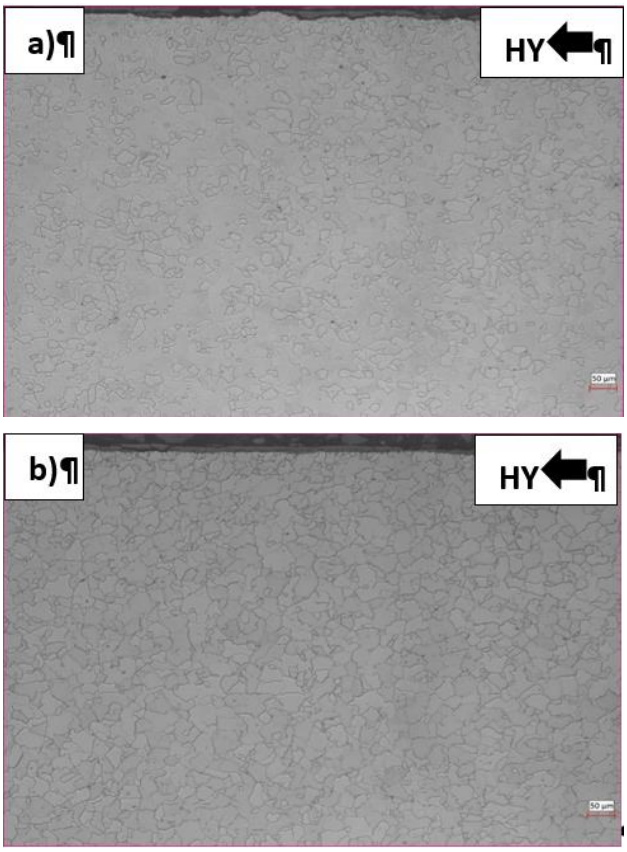

Figure 3. Microstructure view of hot rolled (200x) a) A1 and b) A2 sample

As a result of the microscopic examinations for the 2 mm and 3 mm thick samples taken from hot rolled IF quality steel, the grain size is 9.5 ASTM levels according to the ASTM E112 standard. The grains are arranged along the rolling direction as stated in the literature. The deformation structure is clearly visible. The grains are elongated in the rolling direction. As can be seen from the microstructure images, large ferrite grains are seen in the structure. No second structure was found.

SEM-EDS analyses were performed with the ZEISS Sigma 300 device. The electron beams sent to the sample surfaces by SEM analysis come into contact with the atoms in the sample, and different peak values about their surfaces show the elements and compounds on the surface of the material.

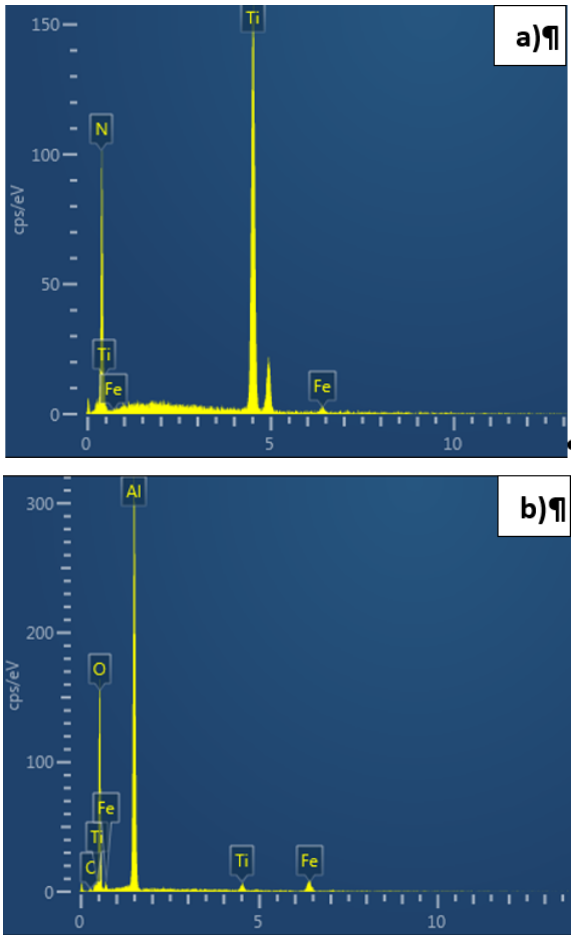

Figure 4. EDS analysis, where amount of Ti: a) increased and b) decreased

When the analysis images made at this point were examined, it was determined that the Ti structure had a maximum peak and N, Fe elements were present. It is seen that precipitates such as Al, oxide is formed with the decrease of Ti amount. It has been observed in this way that the Ti contribution is critical.

6. Conclusion

The aim of this study is to investigate the effect of production process conditions on the chemical and mechanical properties of product and to optimize product quality in IF steels made in EAF, which is used scrap based raw materials. For this purpose, different quality scraps were used with additives such as ferrotitanium. Melted steel was degassed in vacuum, the slab casting process was applied followed by the rolling process. As a result, sheet metal production with optimum width, length and thickness dimensions was achieved. Product characterization was carried out both by chemical analysis, mechanical tests and microstructural examinations. In particular, microstructure investigations have shown that this type of addition is extremely important, since interstitial atoms do not form in this type of titanium-containing steel.

Authors' Contributions

Ali Cem Taşdemir performed experimental execution, writing and editing, while Onuralp Yücel contributed to the study in supervision and editing.

Declaration of Competing Interest

The authors declare that they have no known competing financial interests or personal relationships that could have appeared to influence the work reported in this paper.

Acknowledgement

Authors would like to thank Çolakoğlu Metalurji A.Ş, where I did theese experimental studies, Technical Services and R&D Manager Mr. Muharrem Meral, Quality & Process Managers Mr. Dr. Serkan Oktay and Ms. Ayşe Oran, who provide their help by transferring their technical support and knowledge, and all the employees of the Quality Metallurgy Department.

References

[1] https://www.ispatguru.com/interstitial-free-steels/

[2] S. Yadav, A. Kamal, M. Sinha, S. Ghosh, Recrystallization in commercial grade interstitial-free steel, discussing criticality of martensite and massive ferrite nucleation along with mechanical property, Journal of Materials Research and Technology, Volume 15, 2021, Pages 4750-4757, ISSN 2238-7854, https://doi.org/10.1016/j.jmrt.2021.10.036.

[3] Oran, A., (2015). Sürekli Döküm Tekniğinde Bindirme Yapılan Slab Döküm İçin Tonaj, Kalite Belirleme Çalışması, Yüksek Lisans Tezi, İstanbul Teknik Üniversitesi, Fen Bilimleri Enstitüsü, İstanbul, p 34-48

[4] Boyoğlu, E., (2011). Çelikhane ve Haddehane Notları, Çolakoğlu Metalurji A.Ş, Kocaeli.

[5] Şahintürk, C., (2013) Sürekli Döküm Eğitim Dökümanı, Çolakoğlu Metalurji A.Ş, Kocaeli.

[6] Yaşacan, D.A., Günaydın, Y., Çankaya, S. (2005). Ti ve Nb' lu IF çeliklerin de process şartlarının Lankford değerine (r) olan etkisi. Makine Mühendisleri Odası, Erdemir T.A.Ş Kdz., Zonguldak.

[7] Ruwen Zheng, Renbo Song, Wuyan Fan, Effects of annealing cooling rates on mechanical properties, microstructure and texture in continuous annealed IF steel, Journal of Alloys and Compounds, Volume 692, 2017, Pages 503-514, ISSN 0925-8388, https://doi.org/10.1016/j.jallcom.2016.09.018.

BMSM

Bulletin of Materials Science & Metallurgy

Periodical Scientific Journal of UCTEA Chamber of Metallurgical and Materials Engineers

Volume 1, Issue 1, 2024, Pages 11-15 Received: 11.04.2023 Revised: 12.07.2023 Accepted: 22.01.2024

Research Article

Effect of Calcination Temperature on Crystalline phase and Grain size of ZnO Particles

Mahla Shahsavar Göçmen*, Gabriel Uğurgel, Yiğit Gül, Enes Barış Bilge, Ömer Faruk Uslu, Umut Doğan Gürkan, Gökçe Çiçek Kaya, Mithat Emre Şahbazoğlu, Batuhan Yıldız, Gurur Unan, Kris Terzioğlu, Ayşe Dulda

Department of Materials Science and Nanotechnology Engineering, Yeditepe University, Ataşehir, İstanbul, Türkiye

*Corresponding author's email: mahla.shahsavar@std.yeditepe.edu.tr

Abstract

In today's technology, ZnO as a semiconductor, has emerged as a leading candidate in green environmental management systems, owing to its strong oxidation ability, good photocatalytic properties, and large free-exciton binding energy. ZnO is a cost-effective, stable, and high photocatalytic material with good electrical properties and light transmittance, making it useful for various applications such as solar cells, photocatalysts, and electrical equipment. ZnO, being a photocatalyst, can be used for environmental clean-up efforts such as air purification, water purification, and deodorization. In this study, the zinc oxide (ZnO) was synthesised with a forced hydrolysis method and characterised by different characterization techniques. X-ray diffraction (XRD) was used to investigate the change in phase and crystal structure of ZnO particles at different calcination temperatures. Moreover, the average crystallite size of the particles was calculated at various calcination temperatures, using Scherrer equation. Also Scanning Electron Microscopy (SEM) used to image the surface morphology and size of the particles and it is found that the calcination temperature had a significant effect on the morphology of the particles. Additionally, differential Thermal Analysis (DTA) and Thermogravimetric Analysis (TGA) were used to observe the material transitions and changes in mass as the temperature increased.

Keywords

Calcination, ZnO, Forced Hydrolysis

1. Introduction

ZnO particles are fully attractive due to their unique characteristics including high binding energy, a wide band gap of approximately 3.35 eVis, strong oxidation ability, high photocatalytic, chemical stability, low material cost, and the ability to exhibit photocatalysis in the environment [1]. These promising characteristics of ZnO provide very helpful features in order to overcome the environmental issue. Due to its technological importance in various fields, the properties of ZnO have been the subject of many experimental and theoretical studies in recent years. ZnO, verified as a good candidate for different applications, including in piezoelectric devices [2], solar cells [3], transistors [4], textiles [5], light emitting diodes [6], gas sensors [7], photocatalysts [8], and as antibacterial and antifungal agents [9].

So far, various techniques have been utilised for the synthesis of metal oxide particles, including sol-gel, hydrolysis of inorganic salts, ultrasonic technique, microemulsion, and hydrothermal method, polar and polar solvent systems in the literature [10].

The present study investigates the impact of heating on particle size distribution, with the objective of achieving uniform particle sizes and controlling their dimensions

through controlled thermal processes. In this study, the forced hydrolysis method was chosen due to its simplicity and high yield. The subsequent calcination step, a common practice in the synthesis process, involves heating the precursor material to elevated temperatures to facilitate its transformation into the desired product. Herein, we reported the zinc oxide (ZnO) particles synthesised with a forced hydrolysis method followed by a calcination process under different temperatures at 500 °C, 700 °C, and 900 °C. The phase structure, size, morphology, thermal stability of samples studied by different characterization techniques; X-ray diffraction (XRD), Scanning Electron Microscopy (SEM) Differential Thermal Analysis (DTA) of ZnO particles.

2. Materials and Methods

2.1. Materials

Zinc chloride ($ZnCl_2$), ammonium hydroxide (NH_4OH: ≥%25 NH_3 in H_2O) and distilled water (DI H_2O) were used as all the precursors were used directly without any pre-treatment and further purification.

2.2. Synthesis

The ZnO particles were produced using a forced hydrolysis method. First, 10 g of $ZnCl_2$ dissolved in 200mL distilled-water kept at room temperature while stirring for 5 minutes. In the next step, 10mL of ammonia (NH_4OH) is added dropwise to the solution at the same time pH controlled until achieving pH= 7.0 (The reactions that occur through the experiment have been listed). The white solution obtained as $Zn(OH)_2$ precipitated in the solutions. The result samples have been centrifuged for 10 minutes at 4000 rpm. The washing process repeated several times. To obtain ZnO powders, after the washing process was completed, particles were dried at 60 °C in the vacuum oven. Samples were calcined at different temperatures (rate of 11.3°C/min) 500°C, 700°C and 900°C for 30 minutes. Then, the samples were allowed to cool down to room temperature and grind to obtain the fine ZnO particles. The synthesis process depicted in detail at Figure 1.

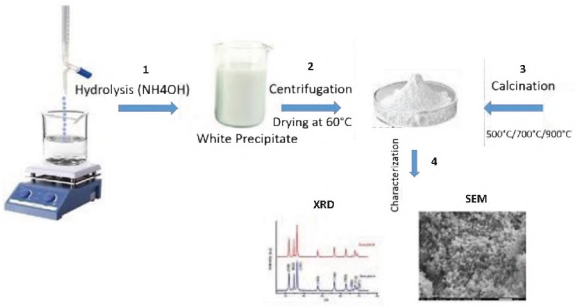

Figure 1. Synthesis and characterization steps of ZnO particles.

3. Measurement and Characterization

The XRD (Bruker D2-Phaser), SEM (Zeiss Evo 40, Leica EM ACE 200 vacuum coater, gold palladium coating), TGA (NETZSCH STA 409 C/CD), and DTA (NETZSCH STA 409 C/CD) techniques were used for the characterization and analysis in this study.

3.1. Characterization

Thermogravimetric analysis (TGA) was used to investigate the thermal stability of samples. The thermogravimetry (TG) curve was obtained in an air flow from 25 °C to 900 °C at a heating rate of 10°C/min. X-ray diffractometer (XRD) with Cu K (λ = 1.5418 Å) source was used to study the crystal structure and morphology of powders. Scanning electron microscope (SEM) characterization was performed under voltage of 15 kV.

4. Results and Discussion

4.1. TGA & DTA Analysis

Figure 2 depicted the TGA/ DTA curves of Simonkolleite ($Zn_5(OH)_8Cl_2 \cdot H_2O$) precipitates which were obtained by hydrolysis of Zinc chloride aqueous solutions with NH_4OH. Significant mass loss steps accompanied by endothermic peaks were observed. The first mass loss (~11%) which was observed in the temperature range 25–135°C was attributed to the removal of adsorbed water. The second and third weight loss (7% and 6%) observed in the temperature range 135–195 °C and 195-250 °C which were assigned to the removal of the intercalated water. The fourth weight loss is assigned to the decomposition and dehydroxylation of hydroxides from Simonkolleite compound between 250-635 °C. The final product of thermal decomposition was found to be ZnO as confirmed by the XRD. The endothermic peaks observed at 135, 195 and 250 °C correspond to removal of water and dehydroxylation of hydroxides, the final endothermic peak can be attributed to the phase decomposition and phase transformation from Simonkolleite to ZnO structure.

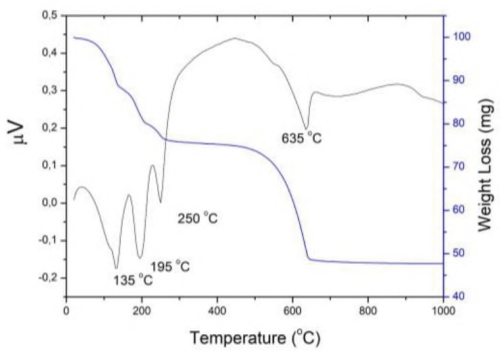

Figure 2. TGA/DTA analysis of simonkolleite ($Zn_5(OH)_8Cl_2 \cdot H_2O$)

4.2. Structural Characterization:

XRD results of the ZnO samples before and after calcination at 500°C, 700°C and 900°C are shown in Figure 3. In order to control particle size and understand growth mechanisms three different firing temperatures (500 °C, 700 °C and 900 °C) were applied for calcination. All peaks before calcination are well matched with Simonkolleite ($Zn_5(OH)_8Cl_2 \cdot H_2O$) structure (JCPDS card no: 007-0155).

According to our synthesis method, when ammonia reacts with water it forms ammonia hydroxide and generates OH– ions as shown in equation (1). These Hydroxyl ions then interacted with Zn^{+4}, leading to the formation of Simonkolleite structures in the presence of chlorine ions as indicated in equation (2) and (3). Although the as-synthesised (white precipitate) samples were washed to remove the chlorine ions, it seems that the washing process was not successful due to the excess of chlorine ions in the system.

$$2NH_4OH_{(s)} \rightarrow 2NH_4^+{}_{(aq)} + 2OH^-{}_{(aq)} \quad (1)$$

$$ZnCl_{2(s)} \rightarrow Zn^{2+}{}_{(aq)} + 2Cl^-{}_{(aq)} \quad (2)$$

$$5Zn^{2+} + 8OH^- + 2Cl^- + H_2O = Zn_5(OH)_8Cl_2.H_2O \quad (3)$$

$$Zn_5(OH)_8Cl_2.H_2O_{(s)} \rightarrow ZnO_{(s)} + H_2O_{(g)} \quad (4)$$

The XRD peaks of samples before calcination and those calcined at 500 °C exhibited a polymorphic structure, in which the graph shows the presence of either Simonkolleite phase structure (marked with *) or ZnO. However, upon increasing the calcination temperature to 700 °C and 900 °C, the XRD peaks confirmed the appearance of pure ZnO crystal structure (JCPDS card no: 036-1451). Notably, significant XRD peaks were observed at angles (2θ) of 31.8°, 34.5°, 36.4°, 47.6°, 56.7°, 62.9°, 68.1°, and 69.3° when the samples were fired at 700 °C and 900 °C, which well matched with ZnO crystal structure. These angles correspond to (100), (002), (101), (102), (110), (103), (200), and (112) planes of ZnO respectively. However, additional peaks shown by stars when the samples were fired at 500°C may indicate the presence of impurities resulting from incomplete phase transformation of the Simonkolleite structure.

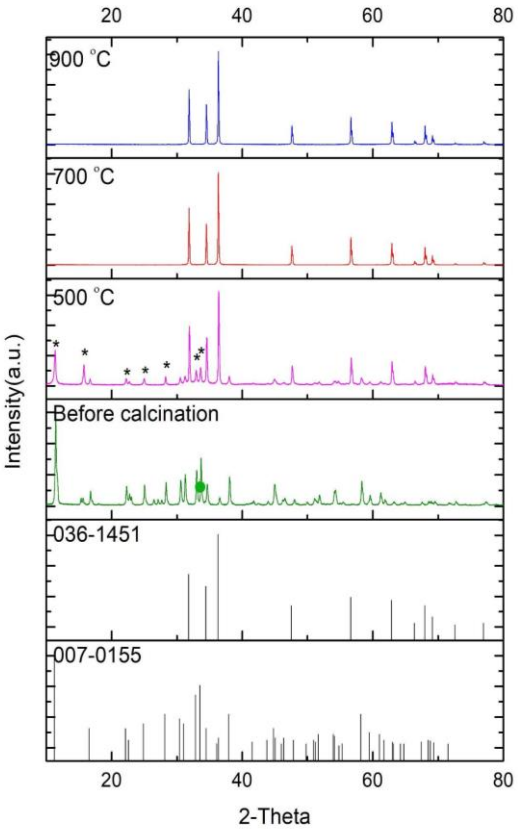

Figure 3. XRD graphs of the standard ZnO particles and as synthesised ZnO particles under different calcination temperatures (Before, 500 °C, 700 °C, 900 °C).

Moreover, average crystallite sizes were calculated, using the Scherrer equation for ZnO particles before and after calcination at 500°C, 700°C and 900°C. The calculation is done by taking FWHM and angle of the most intense peak which corresponds to (101). Average crystallite sizes for ZnO-500, ZnO-700, and ZnO-900 samples were measured as 42.7434 nm, 49.7306 nm, and 50.7144 nm respectively. As expected, the average crystallite size was increased with increasing the calcination temperature. This can be attributed to increased surface energy at high temperature, leading to agglomeration and grain growth.

4.3. Morphological Characterization

The morphology and ZnO particle sizes for all samples were characterised using the SEM (Figure 4). Results showed the shapeless non-uniform particles were obtained when the samples fired at 500 °C, and as the calcination temperature increased to 700 °C and 900 °C clear hexagonal facets started to appear that indicated the formation of ZnO crystal structure

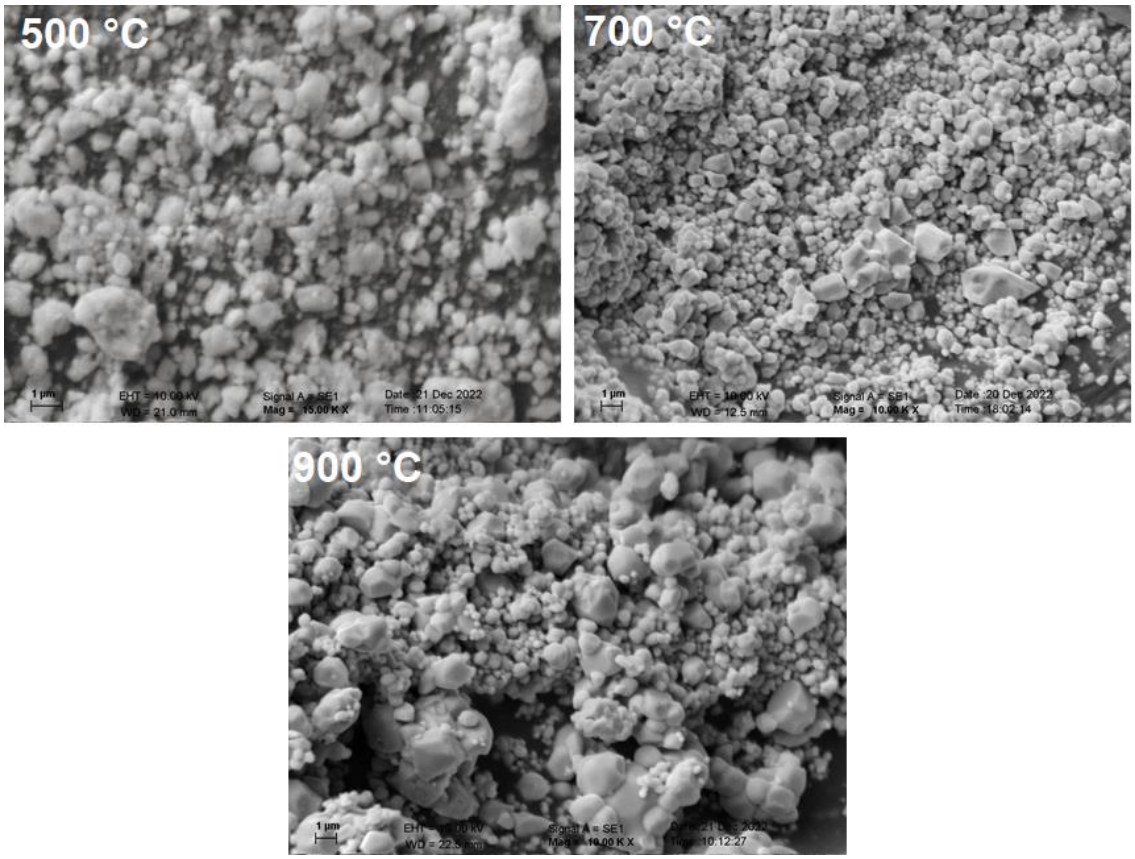

Figure 4. SEM images of the ZnO particles thermally decomposed at 500, 700 and 900 °C.

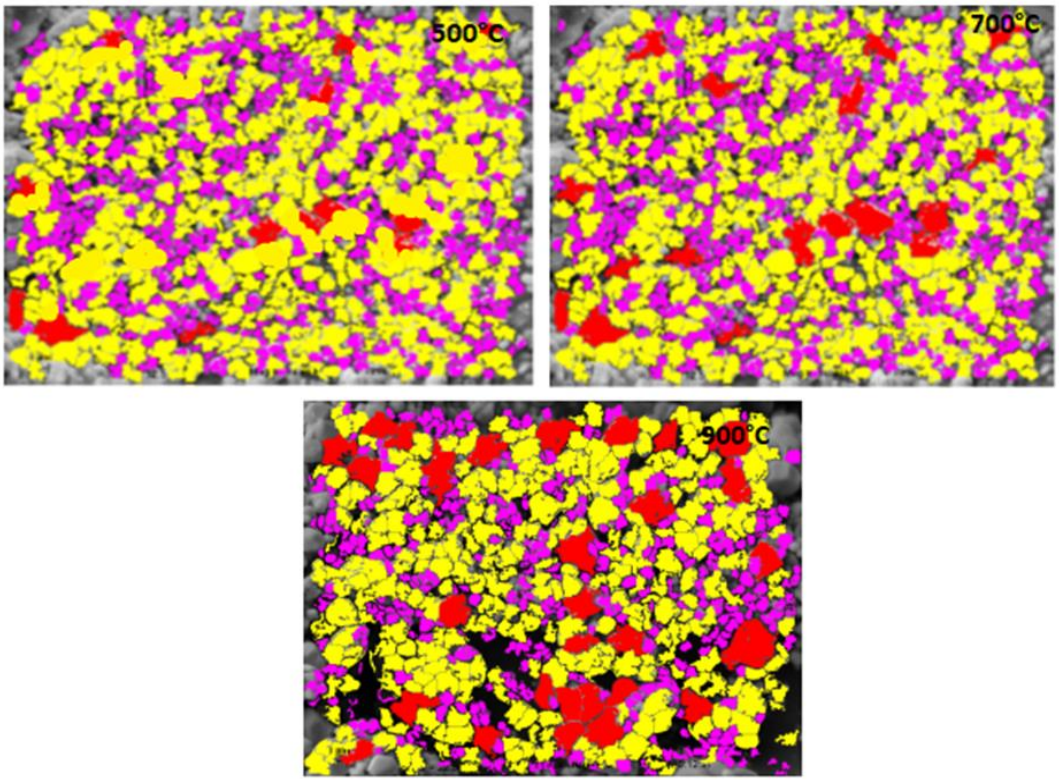

Figure 5. Average particle size in the ranked area of the ZnO particles thermally decomposed at 500, 700 and 900 °C. (Red>Yellow>Purple).

The particle size distribution of the sample was determined by electron microscopy imaging software (Clemex vision lite). The results showed that the sample that measured at 500 °C the small particle size of ZnO was observed and by increasing the temperature to 700 °C and 900 °C the growth takes place in the samples. The average particle size for all samples, in detail, presented in table 1.

Table 1. Estimated structure parameters and average particle size of ZnO particles

Samples	Average particle size (nm)	Maximum (nm)	Minimum (nm)
ZnO- 500	2298 nm	2804.6547	502.8645
ZnO- 700	2308 nm	3203.9472	503.2040
ZnO- 900	2311 nm	3644.2309	503.2051

5. Conclusion

The study concludes that the calcination temperature has a significant effect on the morphology of ZnO particles synthesised using a simple precipitation technique. X-ray diffraction (XRD) was used to analyse the peaks corresponding to different planes of ZnO, and. Using the Scherrer equation, the average crystallite sizes of the particles were calculated at different calcination temperatures, for ZnO particles at 500°C, 700 °C, and 900°C. By using Scherrer Equation, the average sizes of ZnO-500, ZnO-700, and ZnO-900 were found to be 42.7434 nm, 49.7306 nm, and 50.7144 nm respectively. The average sizes of particles increase at elevated temperatures, which might be caused by increasing surface energies that lead to agglomeration of the particles. The study was also characterised by scanning electron microscopy (SEM) to image the surface morphology and particle size distribution. The size of particles was found to approximately range from 2298 nm to 2311 nm with increasing calcination temperature, indicating that the calcination temperature had a significant effect on the morphology and particle size. Additionally, TGA/DTA analysis was performed to deduce the phase transition temperature and thermal stability of samples. The findings indicated that the temperature for the formation of pure ZnO crystalline structure obtained at least 635 °C.

Authors' Contributions

Conceptualization Mahla Shahsavar Gocmen, Ayşe Dulda; methodology Yiğit Gül, Mithat Emre Şahbazoğlu; investigation Gabriel Uğurgel, Enes Barış Bilge, Umut Doğan Gürkan; resources Gökçe Çiçek Kaya, Ömer Faruk Uslu, Batuhan Yıldız, Gurur Unan, Kris Terzioğlu; data curation Mahla Shahvar Gocmen; writing Mahla Shahsavar Gocmen; writing-review and editing Mahla Shahsavar Gocmen, Ayse Dulda; supervision Ayse Dulda.

Declaration of Competing Interest

The authors declare that they have no known competing financial interests or personal relationships that could have appeared to influence the work reported in this paper.

References

[1] D.C. Look, Recent advances in ZnO materials and devices, Materials Science and Engineering: B, Volume 80, Issues 1–3, 2001, Pages 383-387, ISSN 0921-5107, https://doi.org/10.1016/S0921-5107(00)00604-8.

[2] R. K. Pandey, J. Dutta, S. Brahma, B. Rao, and C. P. Liu, Review on ZnO-based piezotronics and piezoelectric nanogenerators: Aspects of piezopotential and screening effect Journal of Physics: Materials, Volume 4, Number 4, 10.1088/2515-7639/ac130a.

[3] Rabisankar Dash, C. Mahender, Prasanta Kumar Sahoo, Ankur Soam, Preparation of ZnO layer for solar cell application, Materials Today: Proceedings, Volume 41, Part 2, 2021, Pages 161-164, ISSN 2214-7853, https://doi.org/10.1016/j.matpr.2020.08.448.

[4] L. Jiang, J. Li, K. Huang, S. Li, Q. Wang, Z. Sun, T. Mei, L. Zhang, N. Wang, X. Wang, Low-Temperature and Solution-Processable Zinc Oxide Transistors for Transparent Electronics, ACS Omega, vol. 2, no. 12, pp. 8990–8996, Dec. 2017, 10.1021/acsomega.7b01420.

[5] Hu, R., Yang, J., Yang, P. et al. Fabrication of ZnO@Cotton fabric with anti-bacterial and radiation barrier properties using an economical and environmentally friendly method. Cellulose 27, 2901–2911 (2020). https://doi.org/10.1007/s10570-019-02965-1

[6] E. Moyen, J. H. Kim, J. Kim, J. Jang, ZnO Nanoparticles for Quantum-Dot-Based Light-Emitting Diodes, ACS Appl Nano Mater, vol. 3, no. 6, pp. 5203–5211, Jun. 2020, 10.1021/acsanm.0c00639.

[7] Yanli Kang, Feng Yu, Lu Zhang, Wenhao Wang, Long Chen, Yingchun Li, Review of ZnO-based nanomaterials in gas sensors, Solid State Ionics, Volume 360, 2021, 115544, ISSN 0167-2738, https://doi.org/10.1016/j.ssi.2020.115544.

[8] Z. Mirzaeifard, Z. Shariatinia, M. Jourshabani, S. M. Rezaei Darvishi, ZnO Photocatalyst Revisited: Effective Photocatalytic Degradation of Emerging Contaminants Using S-Doped ZnO Nanoparticles under Visible Light Radiation, Ind Eng Chem Res, vol. 59, no. 36, pp. 15894–15911, Sep. 2020, 10.1021/acs.iecr.0c03192.

[9] Babayevska, N., Przysiecka, Ł., Iatsunskyi, I. et al. ZnO size and shape effect on antibacterial activity and cytotoxicity profile. Sci Rep 12, 8148 (2022). https://doi.org/10.1038/s41598-022-12134-3.

[10] Kołodziejczak-Radzimska, A.; Jesionowski, T. Zinc Oxide—From Synthesis to Application: A Review. Materials 2014, 7, 2833-2881. https://doi.org/10.3390/ma7042833.

BMSM

Bulletin of Materials Science & Metallurgy

Periodical Scientific Journal of UCTEA Chamber of Metallurgical and Materials Engineers

Volume 1, Issue 1, 2024, Pages 16-22 Received: 09.05.2023 Revised: 24.05.2023 Accepted: 25.05.2023

Research Article

Imprinting Bone Surface Topography on Cast Metal

Aybüke Üretmen[a]*, Caner Demir[b], Vram Odabaşıoğlu[c], Abdulhalim Kılıç[a]

[a]Department of Molecular Biology and Genetics, Istanbul Technical University, Istanbul, Türkiye

[b]Research and Development Department, Tayf Biotechnology, Istanbul, Türkiye

[c]Teknik Döküm Coating Materials Inc., Istanbul, Türkiye

*Corresponding author's email: uretmen20@itu.edu.tr

Abstract

Chemical and physical features including stiffness and roughness texture of the biomaterials are important factors for in-vitro and in-vivo cell behaviour. Bone mimetic topography of the biomaterials can enhance the cell adhesion, cell proliferation and differentiation, leading to promoted bone tissue regeneration. In this study, a new technique for transferring the topography of the decellularized cortical bone to the cast metal was described. Imprinting efficiency and accuracy were high, as shown with light microscopy and atomic force microscopy. This method will pave the way for the development of new materials for bone tissue engineering.

Keywords

Bone topography, Biomimetic, Topography Imprinting, Moulding, Metal Casting

1. Introduction

In human body, cells proliferate and differentiate in various natural scaffold environments such as hard bones and soft tissues. Different tissues have different physical and chemical properties which determine the behaviour of the cells along with protein interactions. Therefore, biomaterials which are implanted into the body need to carry properties suitable for the tissue type for better biocompatibility. Cell differentiation and proliferation are affected by the physical nature of the external surfaces on which cells are attached. [1, 2] These include stiffness, electrical charge distribution, roughness and topography of the surface. [3, 4] Cell adhesion to surfaces and 3-dimensional positioning according to surface topography rearrange the intracellular matrix of the cell. These rearrangements trigger changes in organelle distribution, protein reorganizations and protein interactions also gene expressions in the cells. [5, 6, 7, 8] Cell movement and migration on a surface with varying roughness distribution cause dynamic changes in cell structure limited by the said surface properties of the materials. [9, 10] These are important aspects in developing biomaterials.

Biomaterials can be developed for different applications and purposes including in-vitro cell or tissue development, in-vivo permanent or transient implants and in-vivo degradable implants. Except transient use of the biomaterials, most of the biomaterials need better cell adhesion and compatible cell-material surface interaction. Recent studies investigate the topographic effects of biomaterials on cell growth, cell orientation and cell differentiation. [11] Based on these knowledge, different physical, chemical or biologic methods are being developed and used to form the material surfaces. These can include chemical etching, high voltage plasma treatment, laser ablation, physical abrasion, biological modifications and polymer imprinting [12, 13, 14, 15, 16].

For bone tissue which is more stiff than other body tissues, both surface topography and material hardness level is important in bone tissue engineering and bone implant development. Imprinting bone surface to different polymers such as PDMS (polydimethylsiloxane) is possible, but they lack the necessary hardness values. This limits the development of harder materials resembling bone. It is a great advantage to develop hard metals with bone structure imprinted on. Hard metal surfaces can be used directly or used as master moulds for developing different types of surfaces. Also, hard metals can be used as master moulds for long term usage and can provide repeatability in the bone mimicking surfaces. For these purposes, we developed a method that can be used to mimic the bone surface on metal. In this paper, a

new method for transferring bone surface topography to cast metal surfaces is explained.

2. Materials and Methods

2.1. Materials

2.1.1. Preparing decellularized bone

Thigh bone of male calf, aged 12 months and slaughtered within 24 hours, was used. Phosphate buffer saline (PBS) was prepared from sodium chloride (Merck, EMSURE), potassium chloride (Merck, EMSURE), potassium dihydrogen phosphate (Merck, EMSURE), di-sodium hydrogen phosphate dihydrate (Merck, EMSURE) for washing steps. Sodium dodecyl sulfate (Merck, Ph. Eur) and ethanol (Merck, Absolute) were used for disrupting cells and dissolving organic cell components. di-Sodium tetraborate (Borax) (%98<) used for cross-linking bone structure. Penicillin/streptomycin (Euroclone) and gentamicin were used as antimicrobial agents.

2.1.2. Imprinting bone surface topography on metal

Silicone jewellery moulding rubber (Castaldo, No shrink pink) was used for imprinting bone topography to create a reusable mould. Mould rubber vulcanizer (Teknik Döküm, VPP12-20) was used to vulcanize rubber. A metal rod and scalpel were used to create wax injection channels in the rubber moulds. Wax (Freeman flakes wax, aqua green) was used to fill the bone cavity in the rubber mold. To melt wax and fill in the rubber mold, wax injection device (Teknik Döküm, MK-2000) was used. An air compressor with adjustable air valve was used to adjust pressure during wax injection. Plaster (Chang Jewellery Powder Co., Ltd. EagleTm) was used to surround wax tree tightly and to form cavities for metal. Mechanical stirrer (Mtops, MS3020) was used to mix plaster and water properly. Vacuum chamber providing vibration (Teknik Döküm VH-1) was used in the plaster casting step. The furnace (Teknik Döküm, DF-422D) was used for melting wax in the plaster and to crystallize the plaster. Brass alloy (Pandora Alloys s.r.l, BR88/12-S, %88 Copper, Zn) was used as a metal to transfer bone topography on it. Vacuum casting device (Teknik Döküm, VD-25V) and electric melting furnace (Vevor, GF1100ND3) were used for casting metal.

2.1.3. Surface topography characterization

Compression test was conducted in CheckWay WDW 20KN. Stereo microscope (SOIF) was used for investigating the bone surface transfer to the wax and brass surface. AFM (Atomic force microscopy) was conducted on bone surfaces and cast metal surfaces. AFM analysis were conducted with Nanomagnetics Instruments model ezAFM. For image processing, GIMP and ImageJ used.

2.2. Methods

2.2.1. Preparing decellularized bone

External surfaces of the bones (cortical) were used for topographic transfer purpose. Bones had a periosteum layer which needed to be removed first by cutting with scalpel and taken out by tissue forceps. Then, thigh bone was cut into blocks with surface sizes approximately 5 mm x 10 mm. Thickness can vary according to the different bone locations, ranging from 8 mm to 13 mm. A tabletop bandsaw was used in the cutting process. After cutting, bone blocks were immersed into PBS, containing %1 penicillin/streptomycin and %1 and gentamicin and waited for 10 minutes. Bones were placed into 50 ml conical centrifuge tubes containing 80-90 ºC deionized water and rolled for 1 minute in high speed and water was discharged. Fresh hot water is filled into the tube and process repeated for 5 times. After this stage, bone blocks can be frozen for long term storage in -20 ºC freezer. Bone can lose its surface hardness in the decellularization process, which can lead to topographic memory loss in the imprinting processes. To overcome this problem, we have developed a crosslinking method to keep bone surface hardness. For crosslinking bone to preserve its structural integrity, %1 (w/v) borax solution is prepared in deionized water which was preheated to 39-40 ºC. Bones were placed in the solution and heated to 80 ºC slowly to prevent temperature shock, and kept at that temperature for 4 hours. On-off vacuum cycles were applied for better penetration of the solution into the bone structure and for more effective cleaning of the complex bone structures. In this process, vacuum at 0.1 bar was applied instantaneously using a manual valve, from a vacuum chamber into the vacuum oven. This was repeated with 15 minutes intervals. Between steps, vacuum is kept at 0.4 bar to keep water boiling in low pressure.

After heating process, solution was removed by filtration and bones were rinsed with deionized water. Bones were placed into tubes containing deionized water and vortexed at high speed for 1 minute. Water is discharged and bones were immersed into fresh deionized water preheated to 40 ºC and incubated for 1 hour on the shaker. Water is removed by filtration, and bones were dried on the filtration paper to remove excess water. After these steps, ethanol and SDS solutions were applied to bone blocks to remove cell debris. Bones were immersed into %75 ethanol solution and vortexed for 2 minutes, excess solution is filtered out. Bones were placed into %2.5 SDS solution and incubated for 8 hours at 40 ºC with continuous shaking. After solution is discharged, bones were vortexed in %25 ethanol for 1 minute and incubated in %25 ethanol at 40 ºC for 1 hour while shaking. Vortexing and incubating set was conducted for two times. After filtering out the liquid, the same process was conducted for two times using %75 ethanol solution. Bones were filtered and immersed in absolute ethanol and the process repeated for two times again. To remove ethanol, bones were placed into water and vortexed for 1 minute and incubated in fresh water at 40 ºC for 2 hours. Water was changed at 30 minutes intervals. Bone blocks were immersed in PBS solution,

vortexed for 1 minute and incubated for 30 minutes at 40 ºC by shaking and vortexed again for 1 minute in fresh PBS. Bones were dried at 40 ºC for 2 hours.

2.2.2. Imprinting bone surface topography on metal

To transfer bone surface structure to metal, various steps are necessary.

Transferring bone surface topography to silicone rubber

Bone was used as positive surface pattern and silicon jewellery rubber was used as the first transfer medium for surface topography of the bone. Silicon moulding rubbers were cut and placed in the preheated (200 ºC) rectangular aluminium mould. The bone blocks were placed horizontally on the silicone rubber. Additional layers of silicone rubber were placed on the bone blocks, then the other preheated aluminium mould lid was placed to cover all the rubber layers. This structure was placed into the mould rubber vulcanizer, which was preheated to 155 ºC. In order to activate crosslinking of the rubber, the rubber was vulcanized at 155 ºC for 38 minutes under 6 bar air pressure. After vulcanization, the aluminium mould containing rubber was cooled for 30 minutes in room temperature and the rubber mould was cut in half in the horizontal plane. Bone pieces were removed from the rubber mould carefully. The channels on the silicone rubber mould were carved using a heated metal rod and a scalpel for wax injection.

Transferring surface topography from silicone rubber to wax

The prepared silicone rubber mould was used as an intermediate mould to transfer the bone surface topography to the wax. The injection wax was melted in the pot of the wax injection device at 80 ºC. The injection device was connected to the air compressor to supply air pressure (0.6 bar) to the melted wax. The silicone rubber mould, with the negative pattern of the bone surface topography inside, was pressed against the wax injection nozzle on the device while firmly pressing with metal plates from each side. The melted wax was filled into the cavities through the channels opened in the silicone rubber mould and hardened after approximately 2 minutes. The bone surface topography was transferred to the wax surface. These formed wax moulds were removed from the silicone rubber mould without damaging their surfaces.

Transferring surface topography from wax to plaster

A wax rod was prepared by pouring wax into a thin hollow cylinder and after cooling the wax rod was placed in the middle of a lid. Using a soldering iron at 100 ºC, bone topography imprinted wax moulds were stuck to the wax rod with an acute angle upward to create a wax tree. Upward connection is important for having mostly laminar flow in the metal casting steps to prevent surface distortions. A metal hollow cylinder containing vacuum holes was placed around the wax tree and sealed by the lid from downside. The holes on the cylinder were sealed with a tape before the plaster was cast to prevent leakage. The cylinder containing tree was placed inside the vacuum vibration chamber.

To prepare plaster, 1220 millilitres of water was measured, 3050 grams of plaster powder was weighted and placed on the water for the cylinder with diameter 120 mm and height 200 mm. The water/powder ratio is important for the final strength of the plaster and its porosity ratio, which is important for metal casting process. Water and plaster powder were mixed first with a glass rod and then with a mechanical stirrer for 4 minutes. Vacuum was applied to the plaster mixture for 1 minute to remove air bubbles. After this step, the cylinder flask which was in the vacuum chamber was filled with plaster solution. Vacuum and vibration were immediately applied to the chamber for 2 minutes. The plaster was dried at room temperature for 2 hours and the tape around the flask was removed.

Transferring surface topography from plaster to metal

The dried plaster was placed in the furnace. The furnace temperature was gradually increased to 200 ºC in 1 hour. The temperature was kept at 200 ºC for 2 hours to completely melt the wax and let the wax flow down from the plaster cavities. After 2 hours, the furnace temperature was gradually increased to 730 ºC in 3 hours and maintained at that temperature for 4 hours. Then, the furnace temperature was gradually reduced to 400 ºC before the metal casting step. When the plaster temperature reached to 400 ºC, the cylinder flask was placed in the vacuum casting device. Vacuum was applied before casting metal and during the casting process to prevent air sockets and to allow efficient metal-plaster surface interaction.

The brass alloy was melted in a graphite melting pot at 1110 ºC in the electric melting furnace. The molten alloy was then immediately cast into the plaster and argon gas was applied immediately. When metal colour becomes red, the cylinder flask was taken from the casting device and was dept to the water for cooling. Then, with a hammer and pressurized water (10 bar), the plaster was broken. The metal tree which has the bone surface topography with positive pattern were removed from plaster.

2.2.3. 2.2.3. Surface topography characterization

Compression test was applied with a 1 mm/min rate to 15 mm x 20 mm bone sections. Epoxy resin was applied into the remaining trabecular bone under the cortical bone to prevent crushing. Stereo microscopy was used for investigating the efficiency of bone surface transfer to the wax and brass surfaces. Microscopy photos were processed in ImageJ and GIMP for distinguishing structures better. AFM was conducted on the bone block and cast metal surfaces. For both bone blocks and cast metal, a 40 µm x 40 µm area was examined with a speed of 4 µm/sec. The imaging was conducted in non-contact mode. Gwyddion 2.57-1 software was used to analyse and inspect AFM raw data.

2.3.Results and Discussion

A schematic summary of the developed method for transferring bone surface structures to cast metal can be seen in Figure 1. In the first step involving silicon rubber vulcanization, sufficient pressure must be applied to the mold. Otherwise, it was observed that bone structure was not transferred efficiently to rubber. Also, the type of silicon rubber is important, which affects imprinting details of topographic changes. On the other hand, bone have some structures on its surface which have layered properties and having some sharp-edged. Silicon rubber infiltrates into these areas and fill these volumes and when mold was released from bone some micro particles of the bone surface can be trapped in these areas or rubber can be torn in microscale. To overcome this problem, having a silicon rubber with sufficient stiffness which is in the range 38-45 shore hardness value is necessary. Shrinkage of the silicon mold can increase this problem and can also lead to deformed topography transfer. For this purpose, it was found that no-shrink rubber type was a better choice.

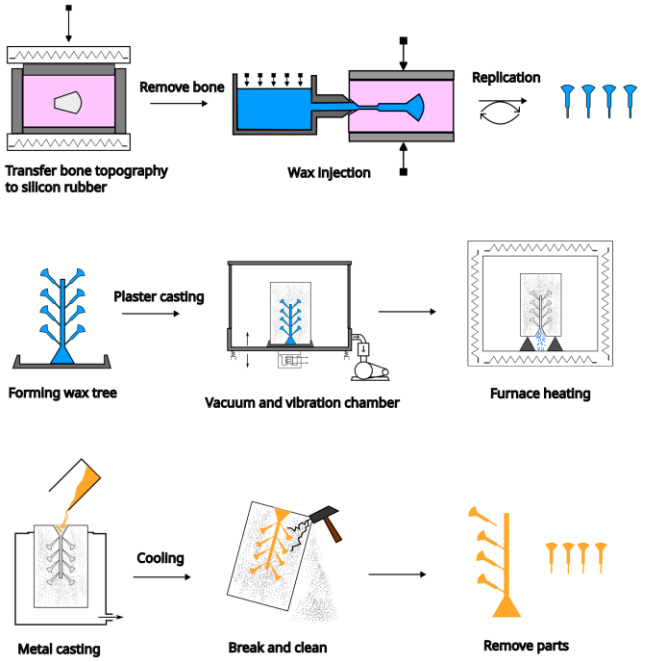

Figure 1. Summary of the process for transferring bone surface topography to metal.

The quality and hardness of the bone after the decellularization process can have an effect on the surface quality of the silicone rubber. Any method involving ultrasonication or other harsh treatment can lead to produce a more brittle and softer surface. This can cause some loss of the topographical properties of the bone from its original state, especially when transferring the bone surface to other surfaces, and can cause micro-particles entrapped in the silicone mould surface. We have developed on-off and continuous vacuum treatment cycles in the decellularization process for more efficient cleaning instead of this method to preserve surface structure. Borax application has been found to preserve the strength of the cortical bone, having 13.3 GPa for natural dry bone and 11.7 GPa for decellularized dry bone, but more importantly, it is the surface hardness of the bone. More analysis must be conducted to measure the surface stiffness with a roughness meter. To explain the effect of borax in terms of chemical reactions, it must be considered that collagen molecules contain functional groups that can react with di-sodium tetraborate (borax). The borate ions in borax can react with the hydroxyl and amino groups present in collagen molecules, resulting in the formation of covalent bonds between the collagen molecules. When borax comes into contact with collagen molecules, it reacts with hydroxyl groups (-OH) present in the amino acid residues of collagen. Specifically, the hydroxyl groups are present on the side chains of three amino acids - proline, hydroxyproline, and lysine - which are commonly found in collagen. Borax reaction with amino acids forms stable covalent linkages between collagen molecules, resulting in crosslinking. Crosslinking of collagen molecules can enhance their stability under high temperature and solvent applications.

After bones were taken out from silicon rubber, any remaining were cleaned with brush and dry air flow. This ensured cleaner surface before wax injection. Using a wax that won't form ash in the heating step of the plaster is important, as ash remaining can decrease cast metal and plaster surface interactions. Silicon rubber containing moulded wax was shown in the figure 2. After forming the tree with these wax moulds and placing the tree into the cylinder filled with plaster afterward, the wax moulds are ready for surface transfer to plaster. The water/powder ratio is important for the final strength of the plaster and its porosity ratio, which is important for metal casting process. Controlled slow temperature increase was applied in the process, as heating is important for having the proper porosity of the plaster without having large hollow areas and cracks. After hardening of the plaster, it is ready for metal casting (Figure 3).

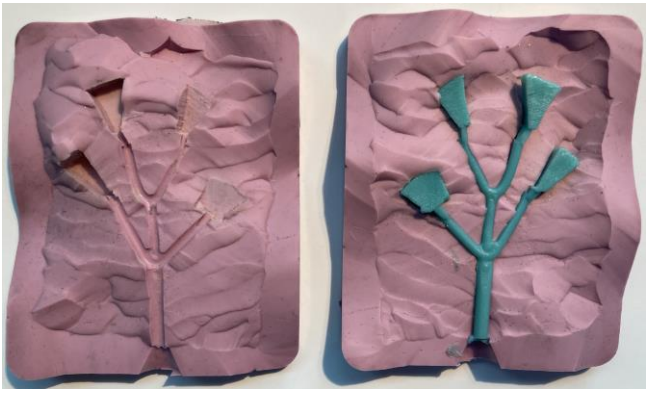

Figure 2. Moulded silicone rubber after filled with wax.

Figure 3. Plaster in the cylinder with holes after hardening and tape removed.

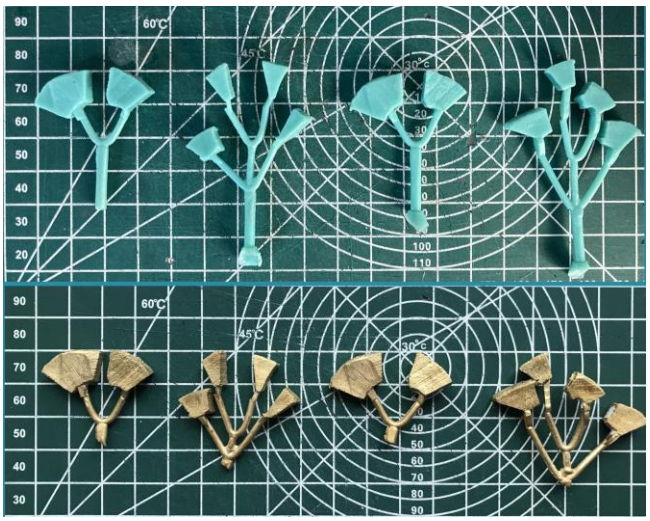

Figure 4. Upper photo with wax moulds before metal casting and lower photo with brass moulds after casting.

In the metal casting process, we have chosen brass for its properties against corrosion and tear, also for its mechanical strength and ease of casting. Before metal casting, the plaster should be in a suitable temperature range to prevent rapid cooling of the metal in the plaster. This ensures the successful transfer of a more detailed surface structure from the plaster to the metal. Plaster temperature is affected by the dimensions of the cylinder, so there is not a fixed temperature for a certain metal. Vacuum application is important in the casting step to ensure complete transfer of plaster surface to metal. Wax moulds before casting and brass moulds after casting were shown in the Figure 4.

Microscopy images show surface structures of natural bone, intermediate wax surface and bone mimicking metal surfaces (Figure 5). There are different macro and microstructures on the natural bone surfaces, which were observed to be transferred onto cast metal. Grooves and peaks were clearly seen in the bone and cast metal surface. It is important to note that though rubber, wax, and plaster were used as intermediate topography transfer mediums, the process had a high efficiency for transferring surface structures. Closer inspection shows characteristic surface properties of certain bone areas transferred to the metal, including sharper edges (Figure 6).

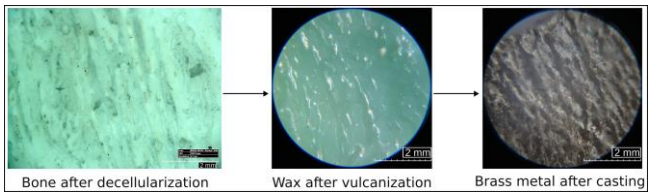

Figure 5. Macro structures on bone, intermediate wax and bone mimetic casted metal. (Scale bar is 2 mm)

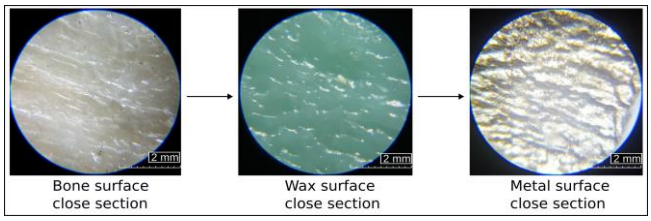

Figure 6. Micro structures on bone, intermediate wax and bone mimetic casted metal. (Scale bar is 2 mm)

There are different surface characteristics which were successfully transferred onto metal surface. As bone surface has a heterogeneous structure in 3-dimensional space, irregular surface topography distribution is expected on metal surface. This distribution can be observed on different areas of the cast metal (Figure 7). A metal stick with a length of 1 mm and thickness of 0.1 mm was placed on the imprinted metal to show macro and micro surface pattern.

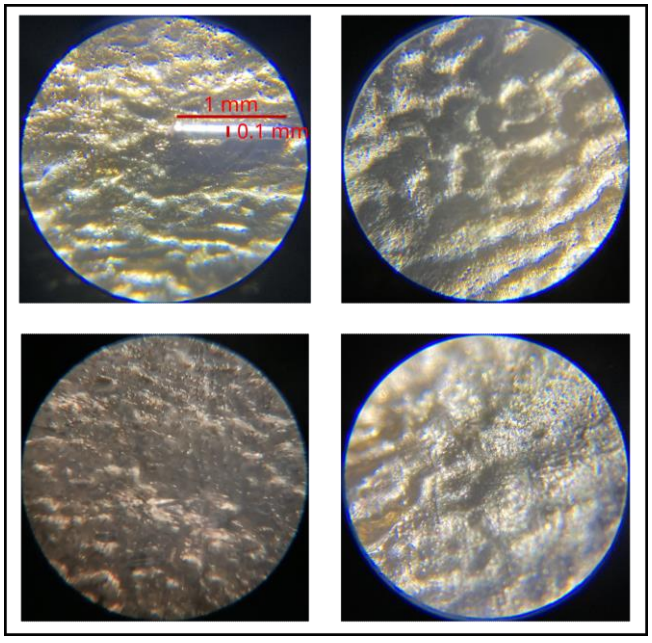

Figure 7. Heterogenous surface topography distribution shown in different areas of casted metal surface. (Scale bar is 1 mm)

AFM analysis has shown that microstructures such as ridges, cavities, and slopes were transferred to the metal surface with a high efficiency (Figure 8). We have examined shallow areas for comparison of bone and metal surfaces to observe microscale transfer efficiency. Roughness average values for

bone and cast metal were 1.382 µm and 1.411 µm, respectively. Root-mean-square roughness values for bone and cast metal were 442.3 nm and 353.9 nm, respectively. Maximum peak height values for bone and cast metal were 1.662 µm and 1.787 µm, respectively. These data show that our process is sensitive and has a high accuracy in terms of topography transfer of bone onto cast metal.

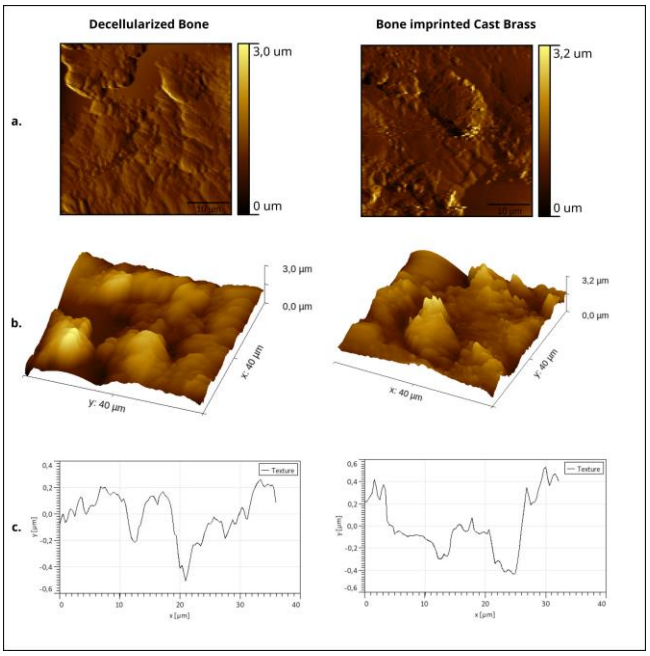

Figure 8. Left column side contains pictures and graph for decellularized bone and right side for cast brass metal. a. 2D AFM images (10 µm scale bar). b. 3D AFM images. c. Roughness texture in random line.

3. Conclusion

A new method for transferring bone topography to hard metal surfaces has been described. This method expands the possibilities for developing new types of bone biomaterials. The method ensures a highly efficient transfer of the bone surface to the cast metal, generally without loss of macro and microstructures. The metal cast bone-mimicking surfaces can be used as moulds for other materials, such as resins, biodegradable polymers, and ceramics. Additionally, metals have high compressive strength, so polymers can be heat pressed onto metal moulds without using solvents, which are typically incompatible for in-vivo applications. Special resins and composite materials can be formed using metal bone moulds for use in in-vitro or in-vivo tissue engineering applications.

For future studies, it is possible to cast high-melting-point metals, such as titanium, with bone-mimicking surfaces that can be used in certain in-vivo implants.

Authors' Contributions

Conceptualization: Aybüke Üretmen, Caner Demir; methodology: Aybüke Üretmen, Vram Odabaşıoğlu, Caner Demir; supervision: Aybüke Üretmen; writing: Aybüke Üretmen; review and editing: Abdulhalim Kılıç; resources: Aybüke Üretmen, Caner Demir, Vram Odabaşıoğlu; materials: Aybüke Üretmen, Caner Demir; data collection: Aybüke Üretmen; literature review: Aybüke Üretmen.

Declaration of Competing Interest

The authors declare that they have no known competing financial interests or personal relationships that could have appeared to influence the work reported in this paper.

Acknowledgement

We thank the company of Teknik Döküm for providing technical instruments and for their technical support.

References

[1] Haihong Liao, Ann-Sofie Andersson, Duncan Sutherland, Sarunas Petronis, Bengt Kasemo, Peter Thomsen, Response of rat osteoblast-like cells to microstructured model surfaces in vitro, Biomaterials, Volume 24, Issue 4, 2003, Pages 649-654, ISSN 0142-9612, https://doi.org/10.1016/S0142-9612(02)00379-4.

[2] Biggs MJ, Richards RG, Gadegaard N, Wilkinson CD, Dalby MJ. The effects of nanoscale pits on primary human osteoblast adhesion formation and cellular spreading. J Mater Sci Mater Med. 2007 Feb;18(2):399-404. doi: 10.1007/s10856-006-0705-6. PMID: 17323174.

[3] Altankov, G., Richau, K. and Groth, T. (2003), The role of surface zeta potential and substratum chemistry for regulation of dermal fibroblasts interaction. Mat.-wiss. u. Werkstofftech., 34: 1120-1128. https://doi.org/10.1002/mawe.200300699.

[4] Han SB, Kim JK, Lee G, Kim DH. Mechanical Properties of Materials for Stem Cell Differentiation. Adv Biosyst. 2020 Nov;4(11):e2000247. doi: 10.1002/adbi.202000247. Epub 2020 Oct 9. PMID: 33035411.

[5] Qian Sun, Qiang Wei, Changsheng Zhao, How do the cells sense and respond to the microenvironment mechanics? Chinese Science Bulletin, Volume 66, Issue 18, 2021, Pages 2303-2311, ISSN 0023-074X, https://doi.org/10.1360/TB-2020-1069.

[6] Wolfenson H, Yang B, Sheetz MP. Steps in Mechanotransduction Pathways that Control Cell Morphology. Annu Rev Physiol. 2019 Feb 10;81:585-605. doi: 10.1146/annurev-physiol-021317-121245. Epub 2018 Nov 7. PMID: 30403543; PMCID: PMC7476682.

[7] Alberto Elosegui-Artola, Xavier Trepat, Pere Roca-Cusachs, Control of Mechanotransduction by Molecular Clutch Dynamics, Trends in Cell Biology, Volume 28, Issue 5, 2018, Pages 356-367, ISSN 0962-8924, https://doi.org/10.1016/j.tcb.2018.01.008.

[8] Fletcher, D., Mullins, R. Cell mechanics and the cytoskeleton. Nature 463, 485–492 (2010). https://doi.org/10.1038/nature08908.

[9] Wong PC, Song SM, Tsai PH, Nien YY, Jang JS, Cheng CK, Chen CH. Relationship between the Surface Roughness of Biodegradable Mg-Based Bulk Metallic Glass and the Osteogenetic Ability of MG63 Osteoblast-Like Cells. Materials (Basel). 2020 Mar 6;13(5):1188. doi: 10.3390/ma13051188. PMID: 32155846; PMCID: PMC7085092.

[10] Lange R, Lüthen F, Beck U, Rychly J, Baumann A, Nebe B. Cell-extracellular matrix interaction and physico-chemical characteristics of titanium surfaces depend on the roughness of the material. Biomol Eng. 2002 Aug;19(2-6):255-61. doi: 10.1016/s1389-0344(02)00047-3. PMID: 12202192.

[11] Qian Sun, Yong Hou, Zhiqin Chu, Qiang Wei, Soft overcomes the hard: Flexible materials adapt to cell adhesion to promote cell mechanotransduction,

Bioactive Materials, Volume 10, 2022, Pages 397-404, ISSN 2452-199X, https://doi.org/10.1016/j.bioactmat.2021.08.026.

[12] Sjöström T, Dalby MJ, Hart A, Tare R, Oreffo RO, Su B. Fabrication of pillar-like titania nanostructures on titanium and their interactions with human skeletal stem cells. Acta Biomater. 2009 Jun;5(5):1433-41. doi: 10.1016/j.actbio.2009.01.007. Epub 2009 Jan 21. PMID: 19208503.

[13] Sjöström T, McNamara LE, Meek RM, Dalby MJ, Su B. 2D and 3D nanopatterning of titanium for enhancing osteoinduction of stem cells at implant surfaces. Adv Healthc Mater. 2013 Sep;2(9):1285-93. doi: 10.1002/adhm.201200353. Epub 2013 Mar 12. PMID: 23495107.

[14] Zhang W, Li Z, Liu Y, Ye D, Li J, Xu L, Wei B, Zhang X, Liu X, Jiang X. Biofunctionalization of a titanium surface with a nano-sawtooth structure regulates the behavior of rat bone marrow mesenchymal stem cells. Int J Nanomedicine. 2012;7:4459-72. doi: 10.2147/IJN.S33575. Epub 2012 Aug 13. PMID: 22927760; PMCID: PMC3422101.

[15] Zhengwei Li, Tianming Du, Changshun Ruan, Xufeng Niu, Bioinspired mineralized collagen scaffolds for bone tissue engineering, Bioactive Materials, Volume 6, Issue 5, 2021, Pages 1491-1511, ISSN 2452-199X, https://doi.org/10.1016/j.bioactmat.2020.11.004.

[16] Niu, Y.; Du, T.; Liu, Y. Biomechanical Characteristics and Analysis Approaches of Bone and Bone Substitute Materials. J. Funct. Biomater. 2023, 14, 212. https://doi.org/10.3390/jfb14040212.

BMSM

Bulletin of Materials Science & Metallurgy

Periodical Scientific Journal of UCTEA Chamber of Metallurgical and Materials Engineers

Volume 1, Issue 1, 2024, Pages 23-30 Received: 18.08.2023 Revised: 19.01.2024 Accepted: 22.01.2024

Research Article

Carbon Capture Performance Enhancement of Solid State Synthesized Li_4SiO_4 Powders by Using Different Kind Steel Slags as SiO_2 Source

Fatih Kutay Mete[a], Kağan Benzeşik[a*], Ahmet Turan[b], Maria Teresa Izquierdo[c], Onuralp Yücel[a]

[a]Faculty of Chemistry & Metallurgy, Metallurgical and Materials Engineering Department, Istanbul Technical University, İstanbul, Turkey;

[b]Materials Science and Nanotechnology Engineering Department, Faculty of Engineering, Yeditepe University, Istanbul, Turkey;

[c]Energy and Environment Department, Instituto de Carboquímica, ICB-CSIC, Zaragoza, Spain

*Corresponding author's email: benzesik@itu.edu.tr

Abstract

The potential of lithium orthosilicate (Li_4SiO_4) as a material to capture carbon dioxide (CO_2) is being explored due to its excellent capture capability and thermal stability. Currently, a significant portion of the world's energy needs are met through the burning of fossil fuels, which leads to an increase in atmospheric CO_2 and contributes to global warming. While fossil fuels will remain the primary source of energy for several more years, it is crucial to develop cost-effective and environmentally friendly technology for large-scale CO_2 capture and storage before its release into the atmosphere in order to mitigate the associated greenhouse effect. This study focuses on optimizing the synthesis of lithium orthosilicate using a solid-state method to enhance CO_2 capture. The research involves assessing the key characteristics of the synthesized material that improve CO_2 capture efficiency. The starting materials used for comparison include lithium carbonate (Li_2CO_3), BF (blast furnace), BOF (blast oxygen furnace) and EAF (electric arc furnace) slags, and pure reagents of silicon dioxide (SiO_2). The effect of process conditions, such as synthesis temperatures ranging from 850 to 950°C and varying holding times of 4, 6, 8, and 10 hours in a muffle furnace, were studied and compared. X-ray diffraction (XRD) analysis was performed to characterize the samples and slags. CO_2 capture performance of the samples were evaluated in thermobalance test under 92 vol% CO_2 (N_2 balance) gas concentration at 600°C. As to conclude, carbon dioxide capturing sorbent material was produced by utilizing the slags generated as a by-product in steel production. Thus, considering the principles of circular economy, a material defined as waste was used as raw material for the production of another product used for lowering atmospheric CO_2 levels.

Keywords

Solid state synthesis; Slag utilization; Carbon Capture; Global Warming

1. Introduction

Global warming, a component of climate change, pertains to the sustained elevation of global temperatures over an extended period. It is a concerning phenomenon driven by the increased concentration of greenhouse gases in the Earth's atmosphere, primarily resulting from human activities such as the combustion of fossil fuels in industrial processes, deforestation, and agricultural practices [1]. These activities contribute to the release of significant amounts of carbon dioxide into the atmosphere.

When carbon dioxide (CO_2) and other air pollutants and greenhouse gases accumulate in the atmosphere, they have the ability to trap heat and solar radiation that would otherwise escape into space. This trapped heat creates a greenhouse effect, leading to a rise in global temperatures and a disruption of the Earth's climate patterns. The consequences of global warming include rising sea levels, more frequent and severe weather events, and adverse effects on ecosystems and biodiversity.

To address the urgent need to mitigate the impact of carbon dioxide emissions, researchers have been actively exploring

various approaches to reduce its concentration in the atmosphere. Several technologies have emerged as potential solutions, including absorption, adsorption, membrane gas separation, and gas hydrate technologies. These methods aim to directly capture carbon dioxide from the air or industrial sources, thereby curbing its contribution to the greenhouse effect.

In the pursuit of more effective carbon capture and storage methods, novel materials are being investigated for their ability to capture and store carbon dioxide. One such material is lithium orthosilicate (Li_4SiO_4), which shows promise due to its high capture capacity for carbon dioxide and its thermal stability. By optimizing the synthesis of lithium orthosilicate and understanding its key characteristics, researchers aim to enhance its efficiency in capturing carbon dioxide, paving the way for a more sustainable and environmentally friendly approach to combating global warming [2].

The exploration of lithium orthosilicate (Li_4SiO_4) and its potential applications has extended beyond its use in lithium-ion batteries and CO_2 doping. This ceramic material has garnered significant attention as a robust sorbent for CO_2 capture due to its immediate absorption and desorption capabilities. Its unique properties enable it to quickly and efficiently capture carbon dioxide from various sources, including industrial emissions and the atmosphere.

The research and development efforts surrounding lithium orthosilicate aim to optimize its performance as a CO_2 sorbent. Researchers are investigating methods to enhance its absorption capacity, improve its stability during cyclic CO_2 capture and release processes, and explore its compatibility with different operating conditions.

The utilization of lithium orthosilicate for CO_2 capture aligns with the global pursuit of sustainable and environmentally friendly technologies. By capturing and storing carbon dioxide, this ceramic material has the potential to mitigate the impacts of greenhouse gas emissions, contributing to the worldwide efforts to combat global warming and climate change.

Moreover, the versatile nature of lithium orthosilicate opens up possibilities for its application in other areas related to carbon capture and utilization. Researchers are exploring its potential in catalytic processes, carbon dioxide conversion into value-added products, and even as a potential component in advanced energy storage systems.

In summary, the ongoing exploration of lithium orthosilicate as a robust CO_2 sorbent showcases its significance in addressing the challenges of global warming. Through further advancements and optimization, this ceramic material holds promise for enabling more efficient and sustainable carbon capture and utilization strategies, ultimately driving us towards a greener and more environmentally conscious future [3, 4].

1.1. Slag and Slag Types

Slag is a glass-like by-product that remains after separating a target metal from the raw ore. Slag is usually composed of metal oxides and silicon dioxide. Slags can include metal sulphides and elemental metals. Significant volumes of waste materials, such as slags, are generated during the iron and steel production process.

1.2. Blast Furnace (BF) Slag

Iron ore, iron scrap, and fluxes, such as limestone and/or dolomite, are introduced into a blast furnace together with coke, serving as fuel, to facilitate the production of iron. Within the furnace, coke undergoes combustion, resulting in the formation of carbon monoxide, which acts upon the iron ore, transforming it into a molten state. This molten iron possesses the capability to be moulded into various iron-based products, although its primary application lies in its utilization as a raw material in the manufacturing of steel. As a by-product of the blast furnace process, slag emerges, representing a non-metallic substance predominantly composed of silicates, aluminosilicates, and calcium-alumina-silicates.

In a study, silica extracted from blast furnace slag by using an acid leaching process was used to prepare Li_4SiO_4 using the solid-state reaction method with Li_2CO_3 at 873°C. At 600-650°C, the adsorption potential in pure CO_2 was 100.8 mg CO_2/g sorbent, and it rose to 98% conversion at 700°C. This was linked to the slag's small particle size and the presence of metal impurities like potassium and calcium [5].

1.3. Basic Oxygen Furnace (BOF) Slag

The slag from a basic oxygen furnace (BOF) has high alkalinity, a high angularity, a hard surface, and relatively good mechanical properties [6]. For every ton of crude steel produced in a BOF, approximately 100–150 kg of slag is extracted as waste, depending on the hot metal condition and steel-making activity. Slag from the BOF process contains approximately half of CaO and is used to flux the oxides of silicon (Si), phosphorus (P), sulphur (S), and manganese (Mn) formed during the liquid steel processing process. These oxides react with the dissolved calcium oxide (CaO) to form the BOF slag. Many steel plants only partly reprocess this solid waste, and a large amount is either discarded or used for ground filling also for cement production for construction[7].

BOF slag is considered to have highly heterogeneous surfaces. The heterogeneity of the BOF slag surface is caused by two factors: geometrical and chemical. Geometrical heterogeneity (porosity) is caused by variations in the size and shape of pores, as well as pits, and vacancies meanwhile the chemical heterogeneity is correlated with different functional groups on the surface as well as different surface contaminants. BOF slag's distinctive adsorption properties are influenced by both chemical and geometrical heterogeneities [8].

1.4. Electric Arc Furnace (EAF) Slag

Electric arc furnace (EAF) slag, a by-product of steelmaking recovered during the oxidizing process, can be used as aggregate in hydraulic concrete. Several studies have been conducted on the characteristics of EAF slag in relation to its use in the building industry, specifically on its material properties, possible expansivity, and chemical reactivity. [9, 10]

EAF slag is a non-metallic by-product composed primarily of silicates and oxides produced during the processing of molten steel. Depending on the ferrous oxide material, raw EAF slag may appear as grey or black lumps. This slag typically has a coarse surface texture. In addition, higher iron content in EAF slag may result in a higher density. [9, 10, 11].

It is well known that EAF slag from various regions and factories may have varying appearances and physical properties, depending on the composition of steel scrap used as feed materials, the form of the furnace, steel grades, and processing processes. Regardless of the variations in chemical compositions, EAF slag usually has Mohs hardness values in the range of 6–7 [11, 12].

Characteristics of BOF slag and EAF slag for CO_2 capture have been studied earlier. In this aforementioned study, CO_2-capture characteristics were compared. It has been found that in general, the higher the temperature, the better the calcium (Ca) conversion of slag. The Ca and MgO content of slag is an important factor in determining CO_2 sorption potential at various temperatures and CO_2 concentrations. Ca use of slag increased with rising temperature in the 400–500°C range, likely due to reaction kinetics and reactive gas diffusion also the exothermic character of the crystallization of $CaCO_3$ as the higher temperatures may impede also a more complete carbonates generation. Though for a 50% and 75% CO_2 concentration for BOF slag and 75% concentration for EAF slag, Ca usage at 550°C was found to be lower than at 500°C. One possible explanation is that the carbonation reaction is driven not only by reaction kinetics but also by reactive gas diffusion. Steel slag is a porous material thus CO_2 will diffuse to the slag's surface and then into the slag's pores to react with CaO. Due to this, the thick product layer of calcium carbonate ($CaCO_3$) will cover the surface of CaO, preventing further interaction of CO_2 molecules with CaO. Also, due to the different molar concentrations of $CaCO_3$ and CaO, the high-volume substance $CaCO_3$ would fill the pores within the slag and reduce the available CaO surface area, slowing the reaction even more. In general, for the two types of steel slag, namely BOF slag and EAF slag, the Ca usage will be at its lowest at 50% CO_2 at 450 and 550°C. Higher values may occur when the CO_2 concentration is smaller, about 10% or higher, which is more than 75%. As a conclusion, in terms of both CO_2 reactivity and Ca usage, EAF slag outperformed BOF slag [13].

2. Materials and Methods

2.1. Materials

Three different slags were used, these slags are named; BF (blast furnace), BOF (basic oxygen furnace) and, EAF (electric arc furnace) slags. These three different slags were obtained from different iron and steel Turkish industries. The chemical compositions of above-mentioned slags are given in the Table 1 below.

Table 1. Chemical compositions of slags (wt.%).

Slag	FeO	SiO_2	CaO	Al_2O_3	MgO	TiO_2	MnO
BF	0.36	37.20	39.55	13.14	5.89	1.56	0.42
BOF	18.43	12.25	48.04	2.12	3.72	0.50	2.80
EAF	23.86	15.06	37.07	6.63	6.40	0.63	4.63

2.2. Method

2.2.1. Solid state synthesis of Li4SiO4 powders

Li_4SiO_4 can be synthesized by the reaction of a homogeneous mixture of lithium carbonate (Li_2CO_3) and silica (SiO_2) in a 2:1 molar ratio. Li_4SiO_4 produced by chemical reaction at solid state is as shown (1). This reaction is the overall reaction for the solid-state synthesis of Li_4SiO_4. Firstly, Li_2SiO_3 forms and this formed Li_2SiO_3 reacts with Li_2CO_3 to result in obtaining Li_4SiO_4.

$$2Li_2CO_3 + SiO_2 \rightarrow Li_4SiO_4 + CO_2 \quad (1)$$

In this work, lithium orthosilicate adsorbents have been prepared based on 10 grams of Li_2CO_3 using three separate slags and pure reagent of SiO_2 as silica sources, and the following step was the preparation of the mixture with a molar ratio of 2.1:1 to avoid evaporation of lithium carbonate at high temperatures. Each sample has been mixed for 30 minutes in a turbula mixer to ensure a homogeneous mixture. The mixtures have been put into alumina boat crucibles for calcination and the calcination has been done in muffle furnace at a temperature range of 750-850-950°C and a time duration (holding time) of 4-6-8-10 hours for varying samples. After cooling down under normal conditions, the samples were grinded with an agate mortar in order to shape them into a powder form for XRD analysis.

In review of Table 2, a comprehensive set of 36 experiments was carried out, encompassing various experimental conditions shown in Table 2. Specifically, among these 36 experiments, 12 were specifically focused on investigating the properties of BF slag, while the remaining 24 experiments were dedicated to the evaluation of other slag types and pure SiO_2 reagent.

To investigate and compare the outcomes, a series of experiments were conducted involving BF (blast furnace) slag, BOF (basic oxygen furnace) slag, and EAF (electric arc

furnace) slag. These experiments were conducted under varying temperatures ranging from 850°C to 950°C, and holding times of 4, 6, 8, and 10 hours. To establish a baseline for comparison, pure SiO_2 reagents were also employed in the study.

Table 2. Experimental parameters.

Experiment No. #	Temperature / Time	SiO_2 Source
1	950°C / 8h	BF
2	950°C / 4h	BF
3	950°C / 6h	BF
4	950°C / 6h	BOF
5	950°C / 10h	BF
6	950°C / 10h	BOF
7	850°C / 10h	BF
8	850°C / 10h	BOF
9	850°C / 8h	BF
10	850°C / 8h	BOF
11	950°C / 10h	SiO_2
12	950°C / 8h	SiO_2
13	850°C / 10h	SiO_2
14	850°C / 8h	SiO_2
15	950°C / 6h	SiO_2
16	950°C / 4h	SiO_2
17	850°C / 6h	SiO_2
18	850°C / 4h	SiO_2
19	950°C / 4h	BOF
20	950°C / 8h	BOF
21	950°C / 4h	EAF
22	950°C / 6h	EAF
23	950°C / 8h	EAF
24	950°C / 10h	EAF
25	850°C / 4h	EAF
26	850°C / 6h	EAF
27	850°C / 8h	EAF
28	850°C / 10h	EAF
29	850°C / 4h	BF
30	850°C / 6h	BF
31	850°C / 6h	BOF
32	850°C / 4h	BOF
33	750°C / 10h	BF
34	750°C / 8h	BF
35	750°C / 6h	BF
36	750°C / 4h	BF

Furthermore, additional experiments were carried out specifically focusing on BF slag at a temperature of 750°C. These experiments included holding times of 4, 6, 8, and 10 hours to further assess the behaviour and properties of BF slag under these specific conditions.

2.2.2. CO_2 uptake tests

The CO_2 sorption performance of synthesized powders was evaluated using a TGA equipment (Setaram Setsys Evolution). First, these samples were treated at 100°C in N_2 atmosphere to eliminate possible previous carbonation. Subsequently, they were heated up to 600°C with an increase rate of 20°C/min. Afterwards, they were again subjected to a 10 minutes long process under N_2 gas. Then, tests were carried out for 2 hours under a flow rate of 65 ml/min with a gas atmosphere of 92 vol% CO_2 (balance N_2).

3. Results and Discussion

3.1. Results of thermodynamical investigations

The thermodynamical modelling for the production of the sorbents was performed using the thermochemical simulation software FactSage 8.1. From Figure 1, it can be said that at 225°C, lithium carbonate and silicon dioxide start to react, their moles are decreasing and lithium metasilicate (Li_2SiO_3) moles are starting to increase which means that Equation (1) takes place and both lithium metasilicate and carbon dioxide starts to form. Then, this carbon dioxide, reacts with the excess lithium and forms lithium carbonate again in between 325°C and 425°C according to simulation. Afterwards, the remaining lithium carbonate reacts with lithium metasilicate and starts to produce lithium orthosilicate and carbon dioxide. This explains the molar increase of carbon dioxide and the formation of lithium orthosilicate at 675°C. The products are lithium orthosilicate, carbon dioxide and excess lithium carbonate due to 2.1:1 molar ratio. Lithium orthosilicate is shown as $(Li_2O)_2(SiO_2)$ in the figure.

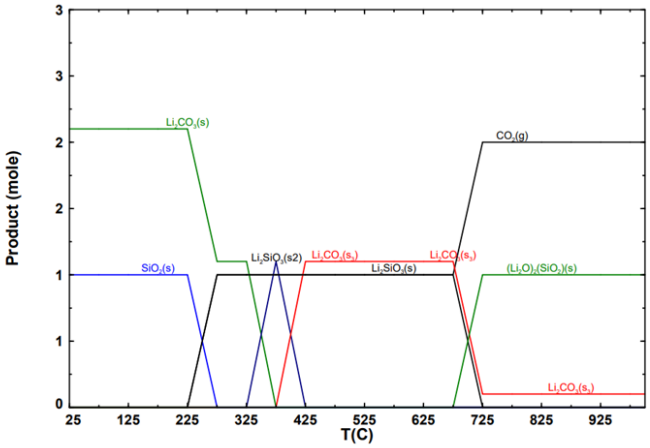

Figure 1. Modelling of the production for Li_4SiO_4 using SiO_2.

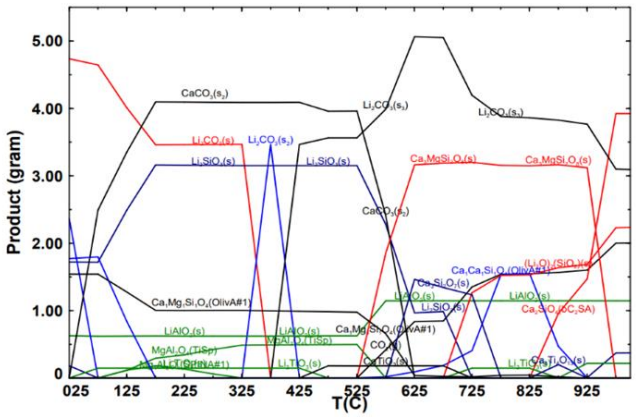

Figure 2. Modelling of the production for Li_4SiO_4 using BF slag.

FactSage makes calculations and simulates the reactions based on closed systems. Slags contain lots of residues and this makes a system very complicated. It can be seen in Figure 2 that the same reaction took place in between 325°C and 425°C, where carbon dioxide, reacts with the excess lithium and forms lithium carbonate, according to simulation. Formation of lithium orthosilicate can also been seen, starting at 675°C. Between 425°C and 475°C, calcium carbonate and lithium titanite reacts to form a small amount of calcium titanite. Then, this calcium titanite starts to react with lithium carbonate at around 675°C to form lithium titanite and thus, calcium titanite converts to lithium titanite. In addition, at 525°C, reaction of lithium carbonate and lithium metasilicate can be seen, after this reaction, carbon dioxide starts to form as it is visible in the figure. It can be seen that the same reaction took place in between 325°C and 425°C, where carbon dioxide, reacts with the excess lithium and forms lithium carbonate, according to simulation.

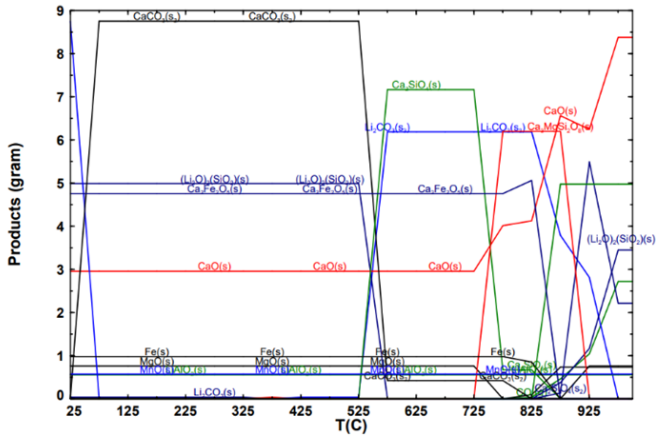

Figure 3. Modelling of the production for Li_4SiO_4 using BOF slag.

According to this simulation, lithium carbonate immediately converts to calcium carbonate without any action and this calcium carbonate starts to form dicalcium silicate and lithium carbonate by reacting with lithium orthosilicate at 525°C. Afterwards, at 725°C, dicalcium silicate reacts with magnesium oxide to form merwinite ($Ca_3MgSi_2O_8$). This simulation has discrepancies and therefore does not reflect accurate information.

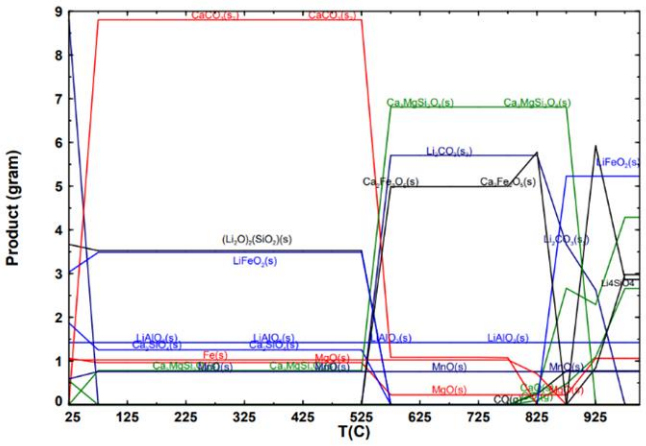

Figure 4. Modelling of the production for Li_4SiO_4 using EAF slag.

In this simulation, calcium carbonate is formed without any interference right at the start from lithium carbonate. At 525°C, calcium carbonate reacts with lithium orthosilicate and lithium ferrite to form merwinite, lithium carbonate, and $Ca_2Fe_3O_5$. At approximately 850°C, $Ca_2Fe_3O_5$ starts to convert to lithium ferrite. At the end, resulting product has lithium ferrite.

Ultimately, it should be noted that FactSage simulates calculations as finite equilibrium. This means that the consistency of these simulations is only consistent if all kinetic conditions are met. In this respect, there might be some inconsistencies.

3.2. Results of solid-state synthesis experiments

Results show that the samples made from BOF with the increasing temperatures decrease the formation of lithium silicates and these samples tend to contain a form of lithium iron oxide. According to the XRD results, with the increase of temperature and decrease of holding time, the samples tend to have more lithium silicate and calcium doped lithium silicates, which improves the CO_2 capture according to other studies made on this topic [3, 14]. The involvement of calcium phases and small quantities of Mg, Fe, and Al in slag-derived lithium silicates may increase both the absorption of CO_2 and the kinetic behaviour and the inclusion of calcium phases in the slag-derived materials explain the variations in CO_2 adsorption capacities between pure Li_4SiO_4 and slag-derived lithium silicates [15].

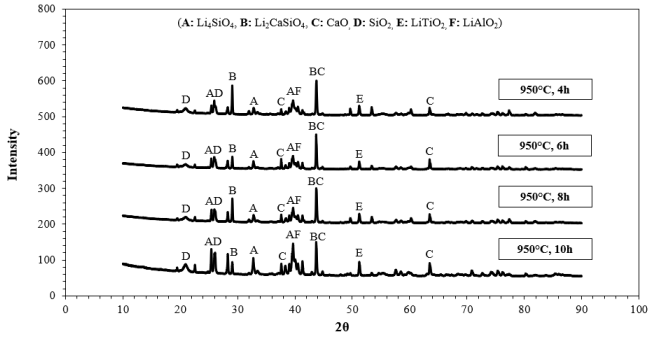

Figure 5. Comparative XRD results for BF slag derived product for 950°C and different holding times.

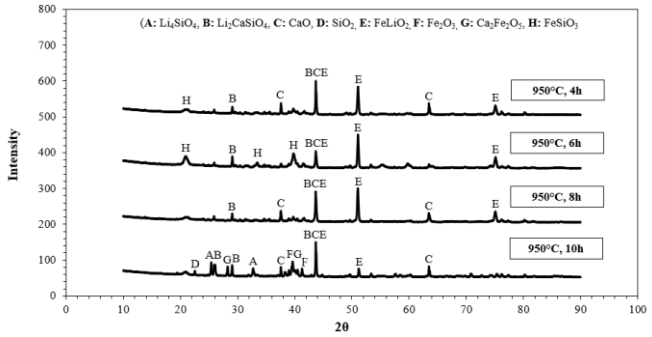

Figure 6. Comparative XRD patterns for BOF slag derived products for 950°C and different holding times.

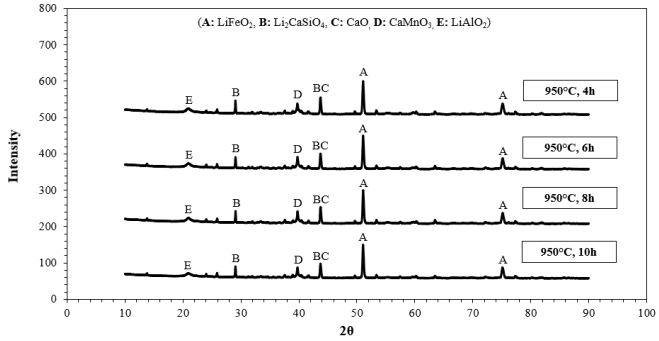

Figure 7. Comparative XRD results for EAF slag derived product for 950°C and different holding times.

The involvement of calcium phases and small quantities of Mg, Fe, and Al in slag-derived lithium silicates may increase both the absorption of CO_2 and the kinetic behaviour and the inclusion of calcium phases in the slag-derived materials explain the variations in CO_2 adsorption capacities between pure Li_4SiO_4 and slag-derived lithium silicates [5].

XRD results show that BF slag-derived samples have much higher lithium orthosilicate (Li_4SiO_4) and dilithium calcium silicate (Li_2CaSiO_4) when compared with other type of slag-derived samples. They also include much less untransformed slag and it can be seen that the conversion rates to lithium orthosilicate (Li_4SiO_4) and dilithium calcium silicate (Li_2CaSiO_4) are satisfying. BF slag-derived samples that are synthesized under 750°C have unconverted lithium carbonate in their compositions. $LiTiO_2$ in small quantities exist in BF slag-derived samples synthesized at 850°C. BOF slag-derived samples that were made at 950°C have a lot of residual materials as it can be seen from XRD peaks. In addition, BOF slag-derived and EAF slag-derived samples have high content of ferrous oxide in their composition. Ferrous oxide hinders the formation of lithium orthosilicate and promotes the formation of lithium ferrite. Because lithium orthosilicate is the main element for capturing large volumes of CO_2 in this study, a low content, or even a complete lack of lithium orthosilicate, limits the performance accordingly. Unlike BOF slag-derived samples, tricalcium silicate content can be seen in EAF slag-derived samples at 850°C. CO_2 reacts with tricalcium silicate; however, it does not have a good uptake performance. This will lead to higher CO_2 uptake and this can be proved by CO_2 uptake tests, which is mentioned in CO_2 uptake results.

Specific surface area determination of the samples was carried out by N_2 physisorption at 77°K by Micromeritics ASAP2020 with performing the Brunauer, Emmett, and Teller (BET) method according to the ISO 9277 Standard. The results for the BET method are given in Table 3.

Exp. No.	Surface Area (m2/g)
7	1.242
9	1.309
30	1.557
5	0.941
1	0.801
3	0.999
34	0.784
14	0.771
12	0.742

Specific surface areas calculated with the BET method are 1.557 m^2/g, 1.309 m^2/g, 1.242 m^2/g, 0.999 m^2/g, 0.941 m^2/g, 0.801 m^2/g, 0.784 m^2/g, 0.771 m^2/g and, 0.742 m^2/g for samples, respectively.

3.3. Results of CO_2 uptake experiments

According to Figure 8, out of these nine samples, the best performance was shown by Sample 30. It reached a value of 14.46% CO_2 uptake at the end of the test. Sample 7, 9 and, 3 almost have the same performance by CO_2 uptake values of 12.58%, 12.65% and, 12.41% respectively.

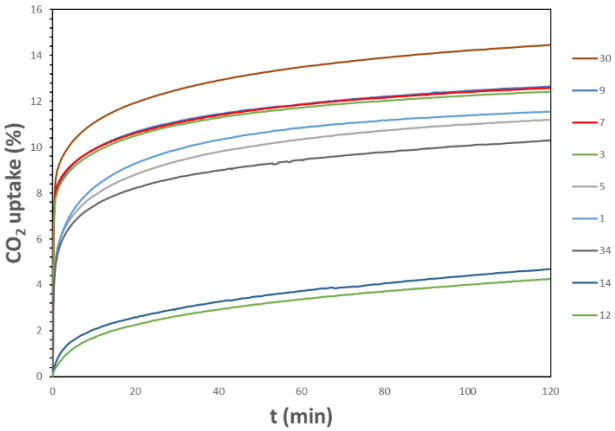

Figure 8. CO_2 uptake values of the samples.

Theoretically, samples that were produced with pure SiO_2 source have 33.78% of CO_2 uptake. However, they performed very poorly compared to samples produced from BF slag as SiO_2 source.

Maximum theoretical CO_2 uptake calculations are made for these samples for 92% CO_2 containing atmosphere and compared to experimental results which can be found below (Table 4).

Table 4. Theoretical and experimental CO_2 uptake values.

Exp. No	Temperature (°C) / Hours	SiO_2 Source	CO_2 Experimental Uptake (wt%)	CO_2 Theoretical Uptake (wt%)
7	850 / 10	BF Slag	12.58	39.26
9	850 / 8	BF Slag	12.65	29.77
30	850 / 6	BF Slag	14.46	40.12
5	950 / 10	BF Slag	11.55	24.47
1	950 / 8	BF Slag	11.19	27.13
3	950 / 6	BF Slag	12.41	35.34
34	750 / 8	BF Slag	10.29	26.03
14	850 / 8	SiO_2	4.69	33.78
12	950 / 8	SiO_2	4.26	33.78

Carbon capture efficiencies of the samples; 32.04%, 42.49%, 36.04%, 64.24%, 51.47%, 46.96%, 39.53%, 13.88%, and 12.61% respectively. Sample 1, which were synthesized at 950°C from BF slag for 8 hours has showed best efficiency by means of comparing with maximum theoretical uptake values while sample 12, which were synthesized at 950°C from pure SiO_2 for 8 hours has showed the worst performance. This confirms that, slag-derived samples are showing greater performance than pure lithium orthosilicate samples made with pure SiO_2 source. The low carbon capture efficiencies of pure SiO_2 samples are likely attributable to the long treatment periods used during synthesis, which has resulted in increased crystal diameter [16]. These results are also in good agreement with the BET results.

4. Conclusion

In this work, lithium orthosilicate adsorbents were effectively synthesized employing three different steel slags which are BF, BOF and EAF as silica sources in addition to pure SiO_2 for comparison. The produced materials were also characterized and tested for carbon dioxide (CO_2) uptake. All BF slag-derived samples showed better conversion rates and thus a better CO_2 uptake percentage. It can be said with certainty that lithium orthosilicate (Li_4SiO_4) captures more CO_2 than dilithium calcium silicate (Li_2CaSiO_4). These findings indicate that slag-derived silicates are attractive materials and good candidates for application in high-temperature CO_2 capture processes. Samples produced from BF slag as SiO_2 source at 950°C have the best performance, followed by again BF slag-derived samples which were produced at 850°C and 750°C. At 850°C and 4 hours of holding time, BF slag-derived sample contains 57.9% lithium orthosilicate, 7.7% dilithium calcium silicate, and 21.3% calcium oxide. At 850°C and 6 hours of holding time, BF slag-derived sample contains 70.5% lithium orthosilicate, 6.2% dilithium calcium silicate, and 21.4% calcium oxide. At 850°C and 8 hours of holding time, BF slag-derived sample contains 61.3% lithium orthosilicate, 8.2% dilithium calcium silicate, and 11% calcium oxide. At 850°C and 10 hours of holding time, BF slag-derived sample contains 69.5% lithium orthosilicate, 6.1% dilithium calcium silicate, and 20.7% calcium oxide. As it can be seen, samples produced from BF slag at 850°C have the best conversion rates compared to other samples. This can be explained when the compositions of the slags are reviewed. BF slag has a higher SiO_2 percentage and also less FeO (ferrous oxide) percentage. This high SiO_2 percentage is an important variable since it converted to lithium orthosilicate (Li_4SiO_4) during solid-state synthesis which has a high yield for CO_2 uptake performance. It has been shown that samples synthesized from BOF slag and EAF slag in this study had ineffective and unfavorable conversion rates when compared to samples created with BF slag, which is also supported by Rietveld studies made by HighScore Plus.

Furthermore, BOF slag-derived and EAF slag-derived samples have showed poor conversion rates. This is due to the high content of ferrous oxide of these slags. Ferrous oxide hinders the formation of lithium orthosilicate and promotes the formation of lithium ferrite. Since lithium orthosilicate is the key material to capture high amounts of CO_2, low content, or in some cases lack of lithium orthosilicate, hamstrings potential performance. Unlike BOF slag-derived samples, in EAF slag-derived samples, at 850°C tricalcium silicate formation can be seen. CO_2 reacts with tricalcium silicate; however, it does not have a good uptake performance.

Low carbon capture efficiencies of samples made with pure SiO_2 is probably due to the long treatment times during synthesis and as a result crystal diameter have increased [16].

High temperature during solid-state synthesis may lead to sintering during the synthesis of lithium orthosilicate. This might result in low efficiencies in carbon capture due to synthesized lithium orthosilicates' cores not reacting with carbon dioxide [16].

In addition, in samples synthesized at 750°C, unconverted lithium carbonate (Li_2CO_3) was found in zabuyelite form according to XRD analysis made with HighScore Plus whilst using the same parameters (heating rate and holding time) as other samples. This shows that at lower synthesis temperatures, lithium carbonate content does not have enough time to react fully and also that it needs to be at higher temperatures. Furthermore, the percentage of lithium carbonate in these samples increased with less holding time which means that it is inversely proportional, the higher the holding time, the less content of lithium carbonate. In the carbon dioxide uptake experiments, the blast furnace-derived samples outperformed the two samples made from pure SiO_2 which converted to 100% lithium orthosilicate, by approximately three times.

On the other hand, other SiO_2 containing waste sources such as industrial wastes, glass wastes, and fly ash or natural resources of SiO_2 like rice hulls might be used in pilot experiments in order to increase waste utilization and feasibility. High porosities might help because it will lead to more reactions with carbon dioxide. Addition of potassium can also be considered since it has improved sorption capabilities in some studies. Sol-gel synthesis approach with LiOH might be recommended for a better capture performance according to the data from other studies. Sol-gel synthesis may also increase the surface area and thus would help with capture performance even more. Palletisation might be done, considering that the obtained powders are too fine. Instead of using wastes containing high content of SiO_2, lithium containing wastes might be used to lower costs.

Authors' Contributions

Writing: Kagan Benzeşik, Fatih Kutay Mete; methodology: Ahmet Turan; material characterization: Maria Teresa Izquierdo; Supervision: Onuralp Yücel.

Declaration of Competing Interest

The authors declare that they have no known competing financial interests or personal relationships that could have appeared to influence the work reported in this paper.

References

[1] Climate change: Atmospheric Carbon Dioxide: NOAA Climate.gov. (2020, August 14). Retrieved February, from https://www.climate.gov/news-features/understanding-climate/climate-change-atmospheric-carbon-dioxide

[2] Eleonora Stefanelli, Monica Puccini, Sandra Vitolo, Maurizia Seggiani, CO2 sorption kinetic study and modelling on doped-Li_4SiO_4 under different temperatures and CO_2 partial pressures, Chemical Engineering Journal, Volume 379, 2020, 122307, ISSN 1385-8947, https://doi.org/10.1016/j.cej.2019.122307.

[3] Izquierdo, M. T., Turan, A., García, S., & MarotoValer, M. M. (2018). Optimization of Li_4SiO_4 synthesis conditions by a solid state method for maximum CO_2 capture at high temperature. Journal of Materials Chemistry A, 6(7), 3249–3257, https://doi.org/10.1039/C7TA08738A.

[4] Benzeşik, K., Turan, A., Yücel, O. (2020). A New Approach for the Production of Li_4SiO_4 Powder. In: Peng, Z., et al. 11th International Symposium on High-Temperature Metallurgical Processing. The Minerals, Metals & Materials Series. Springer, Cham. https://doi.org/10.1007/978-3-030-36540-0_50.

[5] Wang, H., Zhang, J., Wang, G. et al. High-temperature capture of CO_2 by Li4SiO4 prepared with blast furnace slag and kinetic analysis. J Therm Anal Calorim 133, 981–989 (2018). https://doi.org/10.1007/s10973-018-7167-1.

[6] Zongwu Chen, Shaopeng Wu, Yue Xiao, Wenbo Zeng, Mingwei Yi, Jiuming Wan, Effect of hydration and silicone resin on Basic Oxygen Furnace slag and its asphalt mixture, Journal of Cleaner Production, Volume 112, Part 1, 2016, Pages 392-400, ISSN 0959-6526, https://doi.org/10.1016/j.jclepro.2015.09.041.

[7] A. Srinivasa Reddy, R.K. Pradhan, Sanjay Chandra, Utilization of Basic Oxygen Furnace (BOF) slag in the production of a hydraulic cement binder, International Journal of Mineral Processing, Volume 79, Issue 2, 2006, Pages 98-105, ISSN 0301-7516, https://doi.org/10.1016/j.minpro.2006.01.001.

[8] Yongjie Xue, Haobo Hou, Shujing Zhu, Characteristics and mechanisms of phosphate adsorption onto basic oxygen furnace slag, Journal of Hazardous Materials, Volume 162, Issues 2–3, 2009, Pages 973-980, ISSN 0304-3894, https://doi.org/10.1016/j.jhazmat.2008.05.131.

[9] Carlo Pellegrino, Vittorio Gaddo, Mechanical and durability characteristics of concrete containing EAF slag as aggregate, Cement and Concrete Composites, Volume 31, Issue 9, 2009, Pages 663-671, ISSN 0958-9465, https://doi.org/10.1016/j.cemconcomp.2009.05.006.

[10] Samir I. Abu-Eishah, Amr S. El-Dieb, Mostafa S. Bedir, Performance of concrete mixtures made with electric arc furnace (EAF) steel slag aggregate produced in the Arabian Gulf region, Construction and Building Materials, Volume 34, 2012, Pages 249-256, ISSN 0950-0618, https://doi.org/10.1016/j.conbuildmat.2012.02.012.

[11] Teo, P.T.; Zakaria, S.K.; Salleh, S.Z.; Taib, M.A.A.; Mohd Sharif, N.; Abu Seman, A.; Mohamed, J.J.; Yusoff, M.; Yusoff, A.H.; Mohamad, M.; et al. Assessment of Electric Arc Furnace (EAF) Steel Slag Waste's Recycling Options into Value Added Green Products: A Review. Metals 2020, 10, 1347. https://doi.org/10.3390/met10101347.

[12] Grubeša, I.N.; Barisic, I.; Fucic, A.; Bansode, S.S. Characteristics and Uses of Steel Slag in Building Construction; Elsevier Woodhead Publishing: Chennai, India, 2016; ISBN 9780081003688

[13] Yu, J., & Wang, K. (2011). Study on Characteristics of Steel Slag for CO_2 Capture. Energy & Fuels, 25 (11), 5483–5492, https://doi.org/10.1021/ef2004255.

[14] D. Vollath, H. Wedemeyer, E. Günther, Improved methods for fabrication of lithium silicates, Journal of Nuclear Materials, Volumes 133–134, 1985, Pages 221-225, ISSN 0022-3115, https://doi.org/10.1016/0022-3115(85)90138-2.

[15] Alcántar-Vázquez, BC., Ramírez-Zamora, RM. Lithium silicates synthetized from iron and steel slags as high temperature CO_2 adsorbent materials. Adsorption 26, 687–699 (2020). https://doi.org/10.1007/s10450-019-00198-z.

[16] Kagan Benzesik, Ahmet Turan, Şeref Sönmez, Maria Teresa Izquierdo & Onuralp Yücel (2023) Solution combustion synthesis derived Li_4SiO_4 for post-combustion carbon capture, Separation Science and Technology, 58:3, 573-585, DOI: 10.1080/01496395.2022.2136577.

BULLETIN OF MATERIALS SCIENCE AND METALLURGY
Periodical Scientific Journal of UCTEA Chamber of
Metallurgical and Materials Engineers

You may utilize the QR code below to submit a manuscript for the evaluation in the journal.

TMMOB Metalurji ve Malzeme Mühendisleri Odası, Kültür Mahallesi, Çaldıran Sokak Nida Apt. NO:14/13 Kolej, Çankaya-ANKARA / Tel: 0312 425 41 60 / e-posta: info@bulletinofmsm.org

You may take notes on this page.

BULLETIN OF MATERIALS SCIENCE AND METALLURGY
Periodical Scientific Journal of UCTEA Chamber of
Metallurgical and Materials Engineers

TMMOB Metalurji ve Malzeme Mühendisleri Odası, Kültür Mahallesi, Çaldıran Sokak Nida Apt. NO:14/13 Kolej, Çankaya-ANKARA / Tel: 0312 425 41 60 / e-posta: info@bulletinofmsm.org

BULLETIN OF MATERIALS SCIENCE AND METALLURGY

VOLUME 1
ISSUE 1
PAGES 1-30

JAN 2024

ONLINE ISSN:3023-6509

BULLETINOFMSM.ORG